

Probing the timescale dependency of local and global variations in surface air temperature from climate simulations and reconstructions of the last millennia

Beatrice Ellerhoff^{1,*} and Kira Rehfeld^{1,2}

¹*Institute of Environmental Physics, Ruprecht-Karls-Universität Heidelberg, INF 229, 69120 Heidelberg, Germany*

²*now at: Geo- und Umweltforschungszentrum (GUZ),*

Universität Tübingen, Schnarrenbergstr. 94-96, 72076 Tübingen, Germany

(Dated: Published 27 December 2021 in Physical Review E)

Earth's climate can be understood as a dynamical system that changes due to external forcing and internal couplings. Essential climate variables, such as surface air temperature, describe this dynamics. Our current interglacial, the Holocene (11,700 yr ago to today), has been characterized by small variations in global mean temperature prior to anthropogenic warming. However, the mechanisms and spatiotemporal patterns of fluctuations around this mean, called temperature variability, are poorly understood despite their socio-economic relevance for climate change mitigation and adaptation. Here, we examine discrepancies between temperature variability from model simulations and paleoclimate reconstructions by categorizing the scaling behavior of local and global surface air temperature on the timescale of years to centuries. To this end, we contrast power spectral densities (PSD) and their power-law scaling using simulated and observation-based temperature series of the last 6000 yr. We further introduce the spectral gain to disentangle the externally forced and internally generated variability as a function of timescale. It is based on our estimate of the joint PSD of radiative forcing, which exhibits a scale break around the period of 7 yr. We find that local temperature series from paleoclimate reconstructions show a different scaling behavior than simulated ones, with a tendency towards stronger persistence (i.e., correlation between successive values within a time series) on periods of 10 to 200 yr. Conversely, the PSD and spectral gain of global mean temperature are consistent across data sets. Our results point to the limitation of climate models to fully represent local temperature statistics over decades to centuries. By highlighting the key characteristics of temperature variability, we pave a way to better constrain possible changes in temperature variability with global warming and assess future climate risks.

I. INTRODUCTION

The variability of surface air temperature is present on all spatial and temporal scales, from synoptic and seasonal changes to long-term variations on periods of years to multi-millennia. On the one hand, it arises from internal processes, such as the El Niño-Southern Oscillation (ENSO) [1]. On the other hand, the temperature varies due to external forcing, such as the greenhouse effect [2, 3]. Understanding the internally generated and externally forced variability has been suggested to be at least as necessary for evaluating climate risks for society and ecosystems as projecting the global mean temperature [4]. Available instrumental observations are limited to a small time span, leading to challenges in quantifying temperature variability. Paleoclimate reconstructions extend the characterization of temperature variability and can be compared to global circulation models (GCMs) [5–7]. However, discrepancies between model and paleoclimate data remain to be resolved, especially on the local level and on periods between years and centuries [8–12].

Characterizing local temperature variability is crucial for predicting extremes [6], not only to minimize short-term damage but also to design long-term strategies, including urban planning and food cultivation [13]. Vari-

ability of global temperature on periods above years is relevant to the understanding of long-term changes [14] as well as climate sensitivity [15]. Assessing the temporal correlation structure of temperature series by means of scaling behavior and persistence is particularly important for distinguishing externally forced trends from natural changes [16]. It could affect the confidence in future projections and attribution studies [17, 18]. Therefore, one of the main topics to be investigated here is the characteristics of local and global temperature variability on periods of years to centuries from model simulations and observation-based data of the last millennia.

To determine how the variability of a temperature series is distributed with timescales τ , we make use of the power spectral density (PSD) $S(\tau)$, known as “spectrum”. It can be obtained from the Fourier transform of the autocorrelation function (see Appendix A) [19, 20]. The spectrum was shown to often follow a power law

$$S(\tau) \sim \tau^\beta, \quad (1)$$

with spectral exponent β and period τ [21–26], especially on decadal-to-centennial scales [27–29]. We refer to this behavior (1) as temporal scaling since the temperature signal has no preferred timescale and is statistically similar across periods τ . The exact determination of the start and end points of a scaling interval is not part of this study.

Long-range memory stochastic processes are suitable to describe temperature signals with temporal scaling

* beatrice.ellerhoff@iup.uni-heidelberg.de

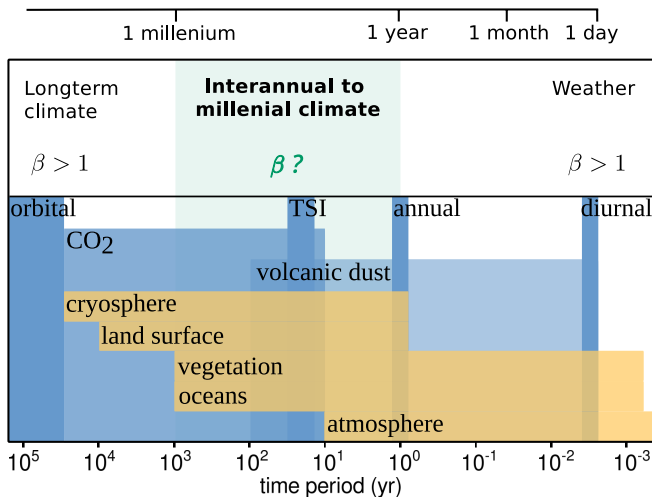


FIG. 1. Characteristic timescales relevant to surface air temperature (T) variability of climatic drivers (dark blue) and climate subsystems (yellow) [32–34]. The weather and long-term climate is characterized by $\beta > 1$ for local and global mean temperature. On interannual to millennial timescales the statistical properties of temperature fluctuations remain to be determined, especially at the local scale. The TSI bar highlights the dominant variations in recent total solar irradiance observations.

[24, 25, 30]. Among those, fractional Gaussian noise (fGn) is a stationary process and exhibits a spectral exponent $\beta \in (-1, 1)$ on sufficiently long periods (see Appendix B). Fractional Brownian motion (fBm) is a non-stationary process that shows $\beta \in (1, 3)$. The scaling exponent β relates to the decay of the autocovariance function (see Appendix B) and indicates how strongly the values within a time series are correlated (or anticorrelated). It is therefore regarded as a measure of the strength of temporal persistence (or antipersistence) [25, 31].

Particular scaling behavior with $\beta \approx 2$ [22, 24] is typical for the weather regime (hours to weeks) and can be explained by atmospheric turbulence [35, 36]. In the long-term climate, regional and global mean temperatures show similar behavior ($\beta > 1$) [23, 24, 29] due to the presence of nonlinear processes, such as the temperature-albedo feedback [37]. On timescales between years to millennia, the temperature is constantly influenced by the interaction of all climate subsystems and by volcanic, solar, as well as CO_2 forcing (Fig. 1). Estimates of the spatially-dependent scaling behavior of local temperature on these timescales differ [24, 27]. On the global scale, many studies find $\beta \approx 1$ [28, 29]. However, Lovejoy *et al.* has identified a change from the so-called macroweather regime ($\beta \approx 0.8$ on periods of 10 days to 40 yr) to the climate regime ($\beta \approx 1.8$ on periods from 40 yr to 80 000 yr) [24].

In this manner, previous works find ambiguity in the interpretation of local and global temperature scaling and it remains to be determined whether simulations

and reconstructions qualitatively agree in scaling behavior $\beta < 1$ or $\beta > 1$. The so-called “ $1/f$ -noise” ($\beta = 1$) corresponds to a process with power spectral density proportional to the period. For $\beta > 1$, the relative contribution

$$\frac{\int_{f'/2}^{f'} S(f) df}{\int_{f'}^{2f'} S(f) df} = \frac{1 - 2^{\beta-1}}{2^{1-\beta} - 1} = 2^{\beta-1} \quad (2)$$

to the variance is larger from slow timescales compared to faster ones for all frequency intervals $f'/2$ to $2f'$ within a scaling interval [38]. With increasing $\beta > 1$, the fBM is said to exhibit “nonlinear pseudo-trends” [30] (see Appendix B). Thus, for understanding climate variability and for modeling purposes, the systematic estimate of the scaling exponent β allows to assess the behavior of fluctuation levels across timescales [25]. Moreover, the differentiation between forced and unforced changes poses a challenge to understanding temperature variability [39, 40]. Beyond the analysis of Haar fluctuations of a few forcing reconstructions [41–43], spectral analysis of climatic drivers and their frequency-dependent linkage to the temperature response remains incomplete.

We investigate the timescale dependency of local and global surface air temperature variability by analyzing power spectral densities from a few hours to a thousand years, thereby extending and improving on earlier work [23, 24, 29, 44]. We use model simulations and observation-based data, which we introduce in Sec. II. To estimate the PSD and determine its power-law scaling on periods of 10 to 200 yr, we use state-of-the-art methods described in Sec. III. This allows us to contrast regional and global spectra (Sec. IV A), spatial patterns (Sec. IV B), and the agreement of simulated and observation-based estimates (Sec. III C). Along with that, we discuss the joint PSD from various radiative forcings, which allows us to calculate the spectral gain and study the externally forced variability in Sec. III D. Based on our reconstruction of the PSD of surface air temperature for the last millennia, we evaluate the consistency of spectral characteristics across the data sets considered. In Sec. V, we elaborate on the stronger persistence of temperature on local than global level as well as remaining discrepancies. Finally, we discuss how our findings could help improve climate model simulations and understand Earth’s climate dynamics.

II. DATA

We investigate the timescale-dependent distribution of surface air temperature variability using model simulations, observation-based data, and radiative forcing reconstructions. The model simulations include ten transient runs from GCM experiments [45]. The observation-based data consists of reanalysis data, instrumental measurements, and the paleoclimate reconstructions from the Past Global Changes 2k (PAGES2k) network [46]. We

use 12 reconstructions of climatic drivers, including solar, volcanic, orbital, and CO₂ forcing. All temperature and radiative forcing signals are specific to the Mid- and Late-Holocene (the last 6000 yr), with a focus on the Common Era (0 to 2000 CE). The supplemental tables S1-S3 [47] summarize their key specifications.

A. Model simulations

Each of the ten GCM runs considered features a transient, albeit different forcing and a comparable spatiotemporal resolution. The CESM-LME 1 [48] and MPI-M LM [49] experiments serve as representative runs of the last millennium. We analyze them at two temporal resolutions (one month, six hours) to capture both the high- and low-frequency variability within our available computing capacities (see Fig. S7 [47]). CESM 1 past 2k [50] is included as a slightly newer run for the Common Era. To cover the Mid-Holocene, we use simulations from the IPSL [51] (denoted IPSL-p6k) and ECHAM5/MPI-OM [52] (denoted ECH5/MPIOM-p6k) of the last 6000 yr. From the TraCE-21k [53] simulation, we also consider only the last 6000 yr to retain comparability and to avoid potential biases due to significant shifts in the mean state of climate. The Mid-Holocene runs were temporally averaged to a bi-monthly resolution to reduce computational costs. To test for the influence of human-induced climate change on our results, we include the HadCM3 LM1 simulation [12], covering the period from 850 to 1850 CE. Furthermore, we compare our results to the pre-industrial (PI) control runs from CESM-LME 1 and MPI-M LM, as well as the TraCE-21k-ORB run, which is solely forced by orbital changes.

B. Observation-based data

In addition to the simulations, we analyze the monthly resolved HadCRUT4 (Hadley Centre/Climatic Research Unit Temperature) instrumental records, ranging from 1850 to 2019 [54]. However, most of the grid-box time series are not available as continuous measurements as required for spectral analysis. Therefore, we retain only those 104 grid boxes with coverage greater than 150 yr after interpolating gaps of up to two months. While the Northern Hemisphere is comparatively well covered up to 72.5°N, only nine grid boxes remain for the Southern Hemisphere. Therefore, this selection comes at the expense of spatial resolution but offers a higher spectral resolution on longer timescales. To further explore the potential effect of these spatiotemporal constraints, we include the ERA5 (European Centre for Medium-Range Weather Forecasts Reanalysis 5th generation) temperature reanalysis for the years 1979 to 2019 [55]. Along with CESM-LME 1 and MPI-M LM, we analyze the ERA5 data at both six-hourly and monthly resolution for the same reasons as mentioned earlier.

TABLE I. Requirements on irregularly sampled time series $x(t)$ for analyzing power-law scaling on timescales $\tau \in [\tau_1, \tau_2]$. We apply this scheme for $\tau_1 = 10$ and $\tau_2 = 200$ yr in Sec. IV B and IV C.

Parameter	Value
Number of data points (N)	≥ 50
Mean temporal resolution ($\langle t_{i+1} - t_i \rangle$)	$\leq \tau_1$
Coverage ($t_N - t_1$)	$\geq 3\tau_2$
Length of hiatuses ($\max(t_{i+1} - t_i)$)	$\leq 5\tau_1$

In addition to direct temperature observations and reanalysis, we analyze paleoclimate data. Paleoclimate records hold preserved biological, chemical, and physical tracers (“proxies”) of past climate. The number of temperature records from paleoclimate data with sub-centennial resolution is limited. Recent progress has been made by improved calibration and pseudo-proxy methods within the PAGES2k network [56]. Therefore, we base our analysis on their newest global multiproxy database for temperature reconstructions of the Common Era [46]. It gathers 692 records from trees, ice, sediment, corals, speleothems, and documentary evidence with a resolution between weeks and centuries. The records are spread over 648 locations, including all continental regions and major ocean basins.

For investigating the variability of global mean surface temperature, we use the seven spatially-weighted statistical reconstructions for the last 2000 yr provided by PAGES2k [46]. To estimate the mean of local spectra, we choose records from the PAGES2k database according to their resolution (≤ 80 yr), their number of data points (≥ 20), their coverage (≥ 20 yr), as well as their maximum hiatuses (≤ 160 yr). To reliably deduce the scaling of the PSD from individual records, we select the records according to our scales of interest (Table I), similar to [25, 57]. Ice core records were excluded from our analysis since they require additional consideration of signal-to-noise ratios at the sub-centennial timescales [58, 59].

C. Radiative forcing

External forcing contributes significantly to temperature variability and is an essential part of reliable climate projections [40, 60, 61]. We study its spectral properties using forcing reconstructions, widely implemented in GCM experiments and coordinated within the Palaeoclimate Model Intercomparison Project (PMIP3/PMIP4) [62, 63]. This includes five solar [64–68], one CO₂ [63] and two volcanic [60, 69] forcing reconstructions as well as Berger’s numerical solution for orbital forcing [70]. Furthermore, we calculate diurnal insolation changes from the hour angle of the sun [71]. We also use a more recently published volcanic [72] and high-resolution solar forcing [73] reconstruction as well as CO₂ measurements [74]. We neglect land-use forcing [75] which is much lower

in amplitude and variability than the other forcings considered here.

All forcing reconstructions are rescaled to radiative forcing equivalents, which express their respective change in the Earth’s radiation balance in Watts per square meter (Wm^{-2}). We apply the widely used formula $5.35 \ln([\text{CO}_2]/278\text{ppm}) \text{Wm}^{-2}$ to rescale CO_2 concentrations $[\text{CO}_2]$, given in parts per million (ppm) [76]. The stratospheric aerosol optical depth (AOD) from volcanic eruptions is rescaled by $(-20)^{-1} \text{Wm}^{-2}/\text{AOD}$ [77], however, the optimal conversion factor is still a matter of debate [78]. Additional uncertainties arise from the wide spread of reconstructions for volcanic and solar forcing. To account for this and the choice of conversion factor, we simulate the joint PSD of radiative forcing by a Monte Carlo approach described in Appendix E. Here, “joint” indicates that the PSD of radiative forcing is calculated by linear summation of the mean PSD from different types of climatic drivers, rescaled to their radiative forcing equivalents.

III. METHODS

Spectral analysis is the primary tool used here for studying the timescale-dependent variability and scaling of temperature series. To minimize uncertainties in the spectral analysis of proxy records, we use state-of-the-art approaches for irregularly sampled time series [79]. Statistical estimators further test for the agreement between simulations and paleoclimate data. We apply linear response theory to derive the spectral gain and investigate the forced temperature response.

A. Spectral analysis

Power spectral analysis requires the assumption that the underlying time series can be described as a weakly stationary, stochastic process with time-independent mean and autocovariance [80]. We therefore linearly detrend all time series as it is standard for temperature analysis [9, 25, 81, 82]. The agreement of the PSD from disjoint time intervals in Fig. S13 [47] provides evidence that stationarity is sufficiently fulfilled. We use the multitaper method with three windows [83, 84] and chi-square distributed uncertainties to compute the PSD. The two lowest frequencies were omitted to reduce biases of the multitaper method [23]. For visual purposes, we apply a logarithmic Gaussian smoothing filter of constant width (0.005 decibels) [85]. Mean spectra were calculated by interpolation to the lowest resolution, binning into equally spaced log-frequency intervals, and taking the average with equal weights [23]. This requires the statistical independence of the averaged values [43]. The spectral exponent β is calculated by linear regression to the logarithm of (1) on periods between $\tau_1 = 10$ and $\tau_2 = 200$ yr after binning the PSD into equally spaced log-frequency

intervals to more uniformly weight the estimate and avoid low-frequency biases [23, 25, 29, 86]. In the case of seven proxy records with an insufficient resolution, the scaling is estimated on their corresponding spectral resolution, but always at least between 20 and 200 yr (Fig. S4 [47]). The uncertainty of the spectral exponent, $\Delta\beta$, is given by the standard error of the linear regression model $\Delta\beta_{lm}$, except for irregularly temperature series.

B. Uncertainties for irregular temperature series

Spectral analysis of proxy records, which are typically not sampled in regular time steps, is more prone to errors than that of regular time series. We aim to minimize biases by accounting for the number of data points, temporal resolution, total coverage, and hiatuses’ length when selecting the records (Table I). We find that the mean temporal resolution of a proxy record approximates well the optimal interpolation time step. Nevertheless, the interpolation introduces uncertainties which are not captured by $\Delta\beta_{lm}$. Similar to Laepple *et al.* [79], we quantify this additional uncertainty $\Delta\beta_{int}$ in four steps: (1) For each record with spectral exponent β , we simulate $N = 100$ surrogate time series with annual resolution and a power-law scaling $\beta_n \approx \beta$ and $n \in [1, N]$. (2) We form the surrogate’s block-average over the proxy record’s irregular time steps and obtain N surrogate time series at record resolution. (3) We interpolate the surrogate time series, calculate the multitaper spectrum, and extract the scaling exponent $\beta_{n,lm}$ from linear regression in the same way as for the proxy record (Fig. S8 [47]). (4) We calculate the mean deviation $\Delta\beta_{int} = \frac{1}{N} \sum_{n=1}^N |\beta_{n,lm} - \beta_n|$ of the ensemble. The uncertainty of the individual fits $\Delta\beta_{n,lm}$ is negligible compared to the mean deviation $\Delta\beta_{int}$. We obtain the uncertainty of the record’s spectral exponent from both, the uncertainty of the initial fit $\Delta\beta_{lm}$ and due to interpolation $\Delta\beta_{int}$ via quadratic summation: $\Delta\beta = \sqrt{(\Delta\beta_{lm})^2 + (\Delta\beta_{int})^2}$.

C. Statistical analysis of spectral exponents

We quantify the agreement of simulated and reconstructed β -values using percent agreement, categorical agreement, and Kappa statistics. Beforehand, we extract the simulated temperature at the proxy record location by bilinear interpolation of neighboring grid boxes to achieve the best possible comparability between record and simulation. Percent agreement p_0 gives the percentage of locations at which the confidence range $\beta \pm \Delta\beta$ from simulation and reconstruction overlap. The agreement by category, here referred to as categorical agreement p_c , is calculated with the help of $\nu = 0.32$, the mean uncertainty of β from all proxy records considered. We then assign the three categories *low* ($\beta < 1 - \nu$), *high* ($1 + \nu \leq \beta$) and *intermediate* ($1 - \nu \leq \beta < 1 + \nu$) to the spectral exponent β . The *intermediate* regime pre-

vents incorrect assignment. To verify the reliability of categorical agreement, we calculate the Kappa statistics

$$\kappa = (p_c - p_e)/(1 - p_e) \quad (3)$$

with expected percent agreement p_e by category [87]. The latter can be obtained from $p_e = \frac{1}{N^2} \sum_{c=1}^3 n_{c,m} n_{c,p}$ where c is the category, N the number of locations and n the number of times that models (m) and proxy records (p) have predicted category c . The κ -coefficient quantifies the reliability from no agreement beyond chance ($\kappa = 0$) to full agreement ($\kappa = 1$). Negative κ indicates agreement that is beyond chance, for example, due to systematic biases.

D. Spectral gain

We investigate how climatic drivers influence the global mean temperature at period τ by calculating the spectral gain

$$G^2(\tau) = \frac{S_T(\tau)}{S_F(\tau)}. \quad (4)$$

Here, $S_T(\tau)$ is the PSD of the global mean temperature and $S_F(\tau)$ the PSD of radiative forcing (see also Appendix C). The gain requires the assumption that the global mean temperature can be well approximated as a linear function of the forcing [26, 88, 89] and that different types of radiative forcing add linearly [90–93]. To this end, we focus on timescales between years and centuries when additivity is a valid assumption and nonlinearities in the global mean temperature are sufficiently small [42, 43]. The main practical problem that confronts us is that the gain might be subject to a sampling bias due to our data sets choice. Therefore, we perform a Monte Carlo simulation of the PSD of radiative forcing and the global mean temperature, as well as the spectral gain as described in Appendix E.

IV. RESULTS AND DISCUSSION

A. Global mean and mean of local spectra

In order to study the timescale dependency of global mean temperature, we present its power spectral density in Fig. 2 (b). It shows the characteristic background continuum, spectral peaks, and higher harmonics associated with the diurnal and annual cycle. Overall, the PSDs tend to agree between the data sets, albeit with some differences on the interannual scale and when compared to the Trace21k ORB run. The Trace21k-ORB run is solely forced by orbital changes and therefore shows less variability than the ensemble mean. The broad spectral peak on interannual periods reveals an artificially amplified ENSO in the shared MPI-M LM and ECHAM5/MPI-OM ocean component [94]. For a better visibility, PI

control runs are separately shown in the supplementary Fig. S6 [47]. Overall, the PSD largely agrees among different data sets, especially towards shorter timescales.

We find a power-law scaling of $\beta \approx 1$ on timescales longer than 10 yr in line with previous results [24, 25, 28]. The PSD decreases more strongly towards shorter periods, which is characteristic of the weather regime [24, 36]. Similar to Nilsen *et al.* [25], we find no evidence for significant changes in scaling behavior around the centennial scale. One limitation of previous work that found scale breaks is that the spectra were estimated across nonstationary shifts in climate, such as the deglaciation [29], and with a change in proxies and archives [23].

We present the area-weighted mean spectra of the local (grid box) temperature in Fig. 2(a). Compared to the global mean in Fig. 2(b), the power increases and the spectral slope decreases, in line with [81]. The spectra agree on periods below 10 yr, except for the artificially amplified ENSO signal mentioned earlier. Moreover, we find a narrow peak at 13 yr, associated with an unrealistic variability in the northern North Atlantic of the TraCE-21k run, similar to [95, 96]. Remarkably, the decadal-to-centennial variability of the reconstructed temperature is increased by one to two orders of magnitude compared to the simulations. The spectral exponent is smaller for models ($\beta < 1$) compared to paleoclimate data ($\beta \approx 1$).

This finding verifies that models show less regional temperature variability and that the mismatch increases towards longer timescales. The results are robust to sampling from the PAGES2k database and the influence of anthropogenic climate change (Fig. S10 [47]). One shortcoming of forming the area-weighted mean PSD is that the uncertainty quantification requires the assumption of independent spatial degrees of freedom of the temperature field. Due to the presence of spatial correlations, an estimate of the effective spatial degrees of freedom and their dependence on the underlying timescale would be needed to resolve this limitation [97].

B. Spatial patterns of persistence

To further investigate the mismatch on local scaling properties, we compare the spatial dependence of temperature persistence from simulations and paleoclimate data in Fig. 3. The simulations largely exhibit small-magnitude scaling exponents ($-1 < \beta < 1$), whereas proxy records were found to also show $\beta > 1$. In this manner, the magnitude of local temperature fluctuations from model simulations often shows no dependence on the decadal-to-centennial timescale. However, approximately half of the proxy records show a variance that grows on increasingly long periods (see also Fig. S11 [47]).

From both simulations and paleoclimate data, we can strengthen the argument by Fredriksen *et al.* [81] that there is no latitudinal dependence of β (Fig. 3), in contrast to previous studies, suggesting a possible linkage

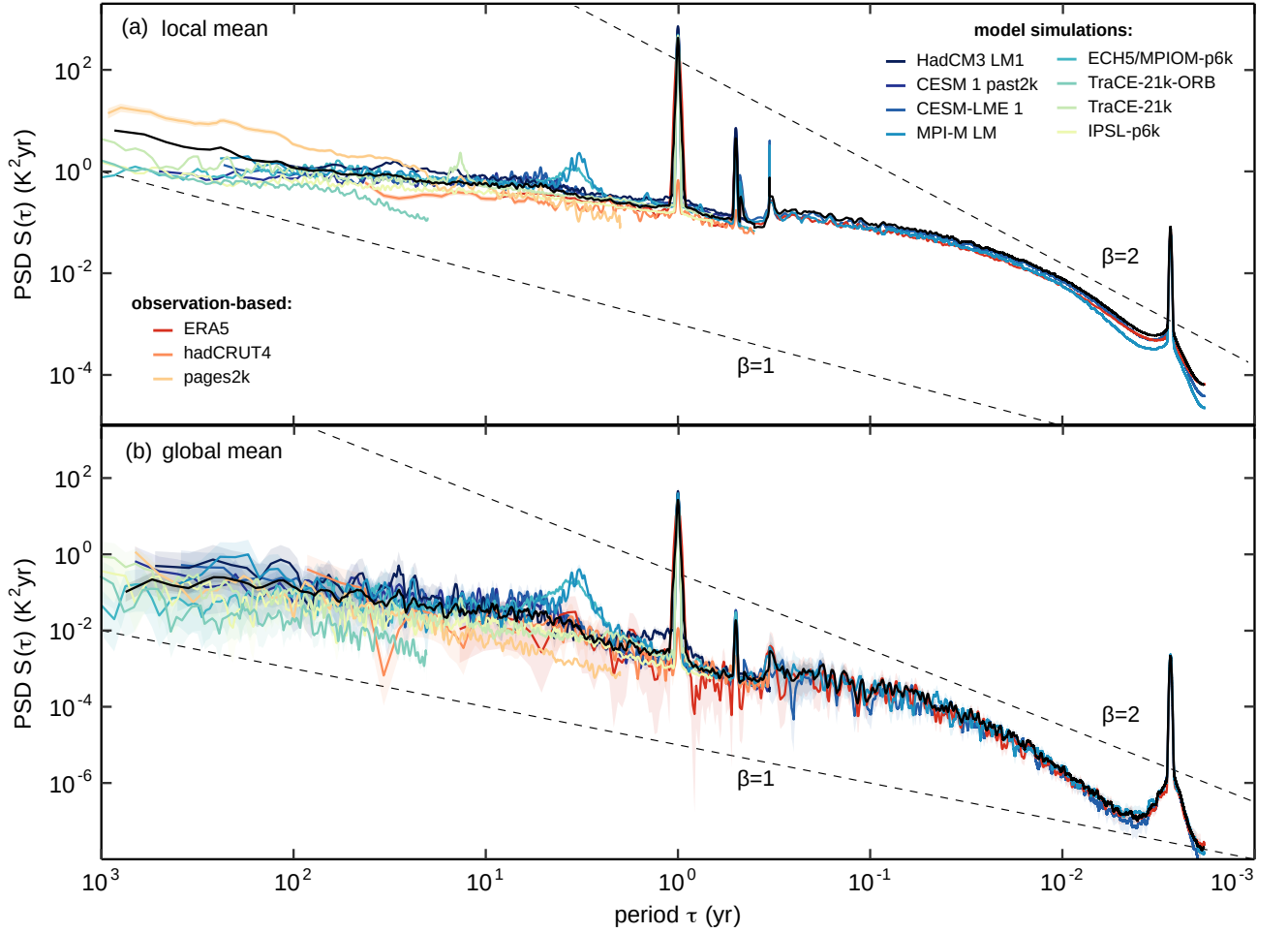


FIG. 2. (a) Mean power spectral densities (PSD) of local temperature from model simulations and observation-based data on periods from hours to 1000 yr for the Holocene. (b) PSD of global mean temperature. The dashed lines with slope β and arbitrary y -intercept in the log-log graph indicate the scaling behavior for visual comparison. The ensemble means (black solid lines) were formed using equal weights across the model group M_0 (see Table S1 [47]).

to the strength of the seasonal cycle [23]. Inspecting the simulations' β -values (background of Fig. 3), we find a small land-sea contrast. Strongest scaling occurs in the Southern Oceans in line with previous findings [81]. Ocean-sea ice interactions with characteristic timescales of the order of centuries and a generally increased internal variability over the oceans might explain these results.

We find generally lower values for the slope β in the ENSO and Indo-Pacific region. This could be attributed to the fact that (quasi-)oscillatory signals, such as active modes of internal variability, are reflected in the PSD as broad peaks and hence cannot be described by a scaling law. On the other hand, this finding is stronger in PI control runs compared to fully forced runs [Fig. 3 (c-f)]. Thus, residual effects of the recent global warming trend might play an additional role [98]. A systematic bias becomes clear from the spatially almost uniform β -values of Trace21k-ORB [Fig. 3 (h)]. In line with Fig. 2, we explain this by the lack of forcing mechanisms on inter-annual to multi-decadal timescales in the aforementioned

simulation.

Marine and lake sediments, as well as the archived documents, follow the general trend of increased β -values compared to simulations. Tree ring records agree well with most simulations in North America and Siberia, but not necessarily at the coast of Australia and northern Europe. Discrepancies such as those in southern South America could reflect the proxies' strength in representing local conditions, for example, topography. However, noise sources in the climate signal recording and preservation, such as bioturbation, can influence proxy records. Further separating the signal content from noise sources in paleoclimate reconstructions can help refine our findings [99, 100].

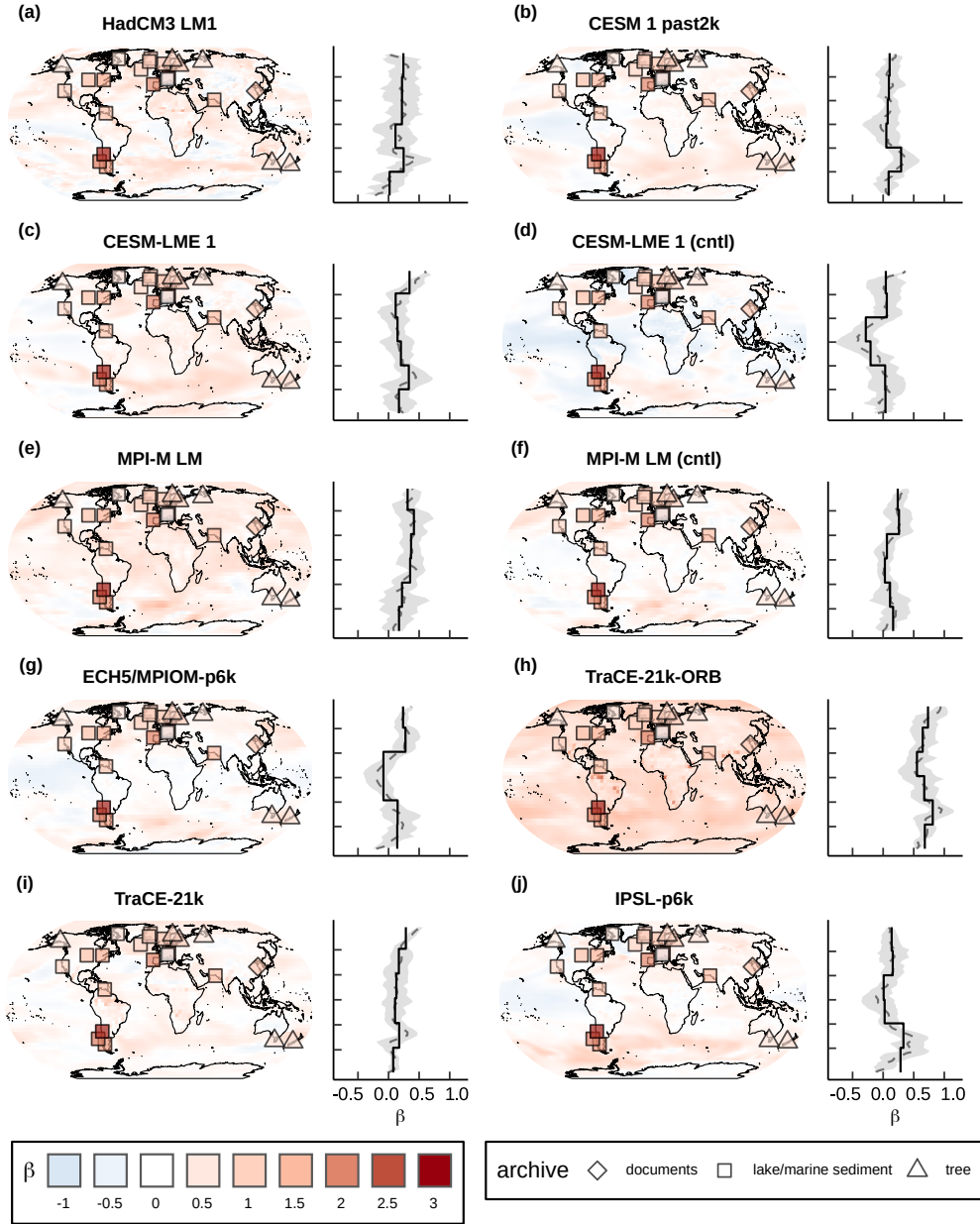


FIG. 3. Local temperature persistence on timescales from $\tau_1 = 10$ to $\tau_2 = 200$ yr across multiple climate simulations and selected proxy records from the PAGES2k database. Colors from blue to red indicate the scaling behavior ranging from $\beta = -1$ to $\beta = 3$. Symbols indicate the scaling of proxy records from different natural archives. The background of each panel shows the β -values fitted to the PSD of the local grid box temperature from simulations. Zonal mean values (dashed curves) are given next to the map, with means (solid curves) over latitude-intervals (with breaks at -60 , -30 , 0 , 30 , and 60° N) and gray shaded confidence intervals. The spatial coverage of proxy records is not sufficient for robust mean estimates, which is why only simulation data are shown here.

C. Statistical agreement of temperature persistence

We further investigate the question of temperature scaling by a statistical analysis of β -values from simulations and paleoclimate reconstructions. It is based on the detailed uncertainty quantification outlined in section III B. Our results show that reconstructions and

simulations agree in less than 30% of locations within the scope of uncertainties (Fig. 4). To single out the scaling behavior of temperature signals, we study the agreement by category. We find approximately 25% of agreement within the categories $\beta < 1 - \nu$ (*low*) and $\beta > 1 + \nu$ (*high*). Although widely accepted [101], categorical and percentage agreement suffer from the limitation to ignore any agreement by chance. Therefore, we investigate the

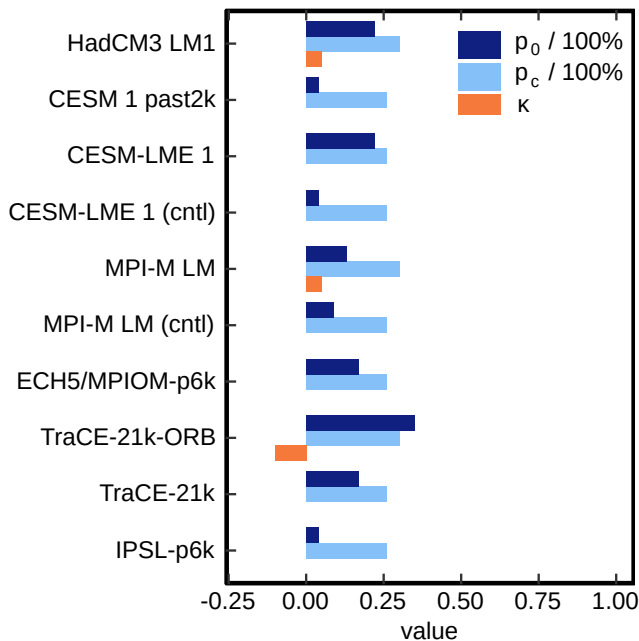


FIG. 4. Percentage agreement p_0 , categorical agreement p_c and inter-rater reliability κ of local temperature persistence from simulations and paleoclimate data. The measures were calculated from a set of bilinearly interpolated simulation records and the proxy record at 23 different locations. Missing orange bars indicate no agreement beyond chance and, therefore, zero inter-rater reliability ($\kappa = 0$).

κ -statistics (orange bar in Fig. 4) and verify that there is no agreement beyond chance ($\kappa = 0$) for almost all models. Only MPI-M LM and HadCM3 LM1 show any, if poor agreement ($\kappa \approx 0.1$), whereas TraCE21k-ORB shows even lower agreement than expected by chance ($\kappa < 0$) due to its systematic bias.

The disagreement could be attributed to both paleoclimate data and simulations. A systematic bias could arise, for example, through the recent, nonstationary global warming trend. Therefore, we repeat our analysis with all time series cut at 1850. In particular, anthropogenic warming slightly increases long-term temperature variability and thus scaling behavior, but not significantly (Figures S6, S9, and S10 [47]). Further uncertainties could arise from our choice of statistical estimator for the scaling exponent β . Maximum likelihood estimation (MLE) should generally be preferred over linear regression (LR) because of its mathematical soundness and skillfulness [102]. We find that MLE is indeed more accurate for regular time series with $\beta > 0$ (Fig. S14 [47]). However, LR allows for estimation of $\beta < 1$, unlike MLE which assumes $\beta > 1$ [102]. In addition, for the characteristics of our empirical data, the differences between the two methods are not significant for $\beta > 0$ (Fig. S15 [47]). Therefore, linear regression represents the preferred estimator for our analysis. Regardless of the chosen estimator, we observe a slight tendency towards

increased scaling exponents for irregularly sampled data (Fig. S15 [47]), similar to Lucke *et al.* [100]. Our uncertainty quantification carefully accounts for these potential errors due to irregular sampling and interpolation by simulating their influence using surrogates (Fig. S8 [47]).

We do not expect other systematic biases for the paleoclimate data since we base our results on multiple archives and proxies, and no systematic spatial pattern is discernible (Fig. S11 [47]). In particular, the cross-correlations between the 23 proxy datasets are weakly positive (0.02 on average with 95% quantiles of -0.17 to 0.21). The assumption of spatial independence necessary for robust statistical analysis (Fig. S16 [47]) therefore appears fully satisfied. The models' resolutions are another possible element of uncertainty that impacts variability over a wide range of timescales [103–105]. We here facilitate inter-model comparison by using state-of-the-art GCMs with comparable spatial and temporal resolutions, but computational costs precluded higher resolutions. The latter might be necessary to improve the representation of decadal variability and response to external forcing. In particular, the increased scaling exponents ($\beta > 1$) from paleoclimate data could indicate that nonlinear processes from an interactive carbon cycle and dynamical ice sheets might not be sufficiently represented in models.

D. The forced temperature response

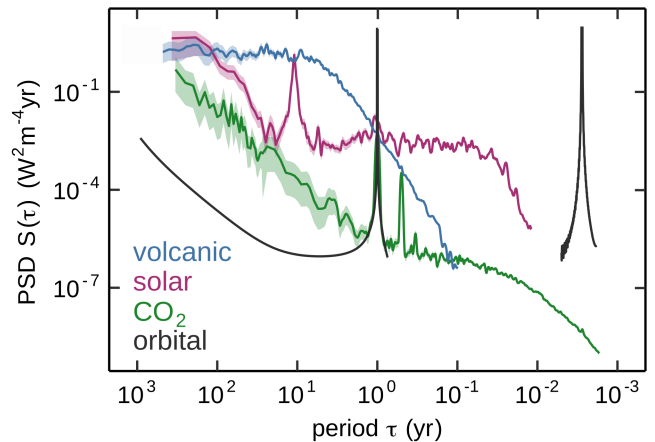


FIG. 5. Power spectral densities from radiative forcings. Details on the reconstructions considered here are summarized in Table S2 and Figure S5 [47].

Climatic drivers are not constant in time and thus affect the surface air temperature on multiple timescales. To investigate the forced temperature response, we present spectra for the main climatic drivers in Fig. 5. The PSD of orbital forcing consists of the diurnal and annual cycle as well as a background continuum on longer timescales. Higher harmonics on monthly timescales were omitted. We calculate the mean volcanic, solar, and

CO₂ spectra using an equally weighted average of spectra from multiple data sets (Fig. S5 [47]). The CO₂ forcing follows the orbital forcing. The PSD of solar forcing again contains more power and has a pronounced peak around the 11 yr solar cycle. Multiple theories and paleoclimate reconstructions suggest the increased variability on centennial to millennial periods due to the long-term behavior of solar activity [106].

Volcanic forcing dominates interannual to centennial scales and undergoes a scale break around the period of 7 yr, estimated using the goodness of fit [102]. Above decadal scales, it follows a white noise spectrum with constant variance. However, the intermittency of volcanic eruptions might have led to biases in the spectral characteristics [42]. We verify our results using an analytical approach described in Appendix D. Remarkably, the derived PSD of an ideal, intermittent time series with Poisson distributed return times explains our findings. We further demonstrate the scale break by a Monte Carlo simulation of the joint PSD of radiative forcing in Fig. 6 (a). This finding raises the question of how the spectrum with a scale break translates into the continuous spectrum in Fig. 2 (b).

We address this question by calculating the spectral gain (4) on periods between years and centuries in Fig. 6 (b). Here, observation-based data include HadCRUT4, ERA5, and PAGES2k again. To account for the model artifacts explained above, we calculate the gain from the model simulation group M_0 and together with group M_+ (see Table S1 [47]). We find that the spectral gain is similar from observation-based data and the model simulation group M_0 , which is the one without artificially amplified ENSO. This suggests that both follow a similar distribution of timescale-dependent variability, as already indicated by Fig. 2(b). Large parts of the gain show constant behavior, which is most pronounced in M_0 . In a simplified way, the gain might be approximated by an ideal linear amplifier or damper of the forcing with comparable internal variability on all timescales. However, we also find a dip around decadal scales, which is strongest in the gain from measurements. Inspecting Fig. 6 (a), this can be explained by forming the ratio between a spectrum with a scale break ($\beta > 1 \rightarrow \beta \approx 0$) and one with moderate scaling ($\beta \approx 1$).

From this standpoint, internal variability slightly grows on periods from years to centuries when slow processes in the oceans, vegetation, land surface, and cryosphere become increasingly active (Fig. 1). While the model simulations follow this general pattern, they may not represent its amplitude correctly, for example, due to the lack of feedback mechanisms. In addition, a too high model diffusivity could cause the suppression of low-frequency variability in model simulations due to a faster energy dissipation over temporal scales [8]. The PAGES2k multiproxy reconstruction, stemming from palaeoclimate data, possibly underestimates internal variability on interannual scales. However, the mean variance ratios in Fig. 5 (b) of the model estimates

agree with those from observations in the global mean. This leaves us with a conundrum: the global mean temperature based on model simulations and observations is mostly consistent in its variability, scaling, and response to forcing. Notwithstanding, locally, the models show a much lower variance on longer timescales and different scaling behavior than reconstructions. Thus, it appears that the statistics of local fluctuations need to be optimized in models but without significantly altering global properties. To this end, the study of unforced (“spontaneous”) oscillations [107] and abrupt transitions [108, 109] in the climate system is one promising approach to improve the representation of local variation. Furthermore, higher-resolved ocean and atmosphere models with additional mechanisms such as ice sheet dynamics and an interactive carbon cycle might increase long-range dependence and persistence of local temperature in the future.

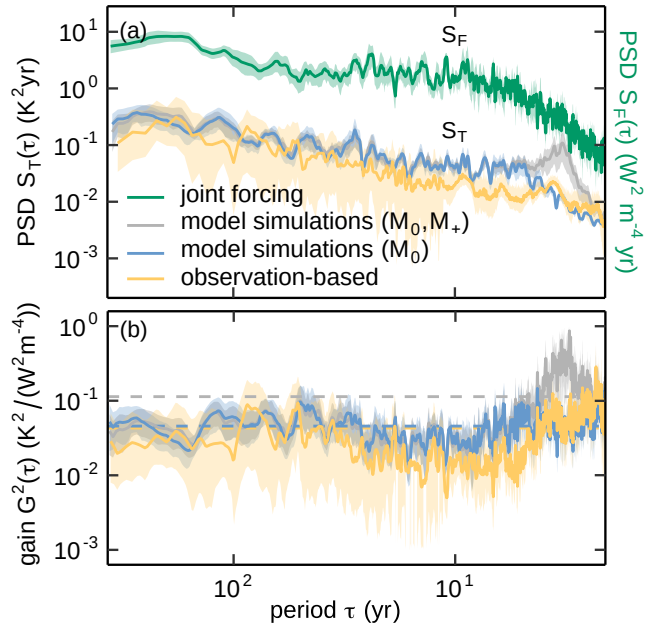


FIG. 6. Monte Carlo simulation of PSD (a) and spectral gain (b) using temperature and forcing reconstructions as well as model simulations. Shaded confidence intervals lie between the 5% and 95 % quantiles. We consider only models from the groups M_0 and M_+ (Table S1 [47]) to exclude model artifacts and to represent the historical temperature response in the best possible way. Notably, M_+ contains those simulations with amplified ENSO [94]. (b) Dashed lines indicate the mean variance ratio $\langle S_T \rangle / \langle S_F \rangle$.

V. CONCLUSION

In summary, we have investigated the question of temperature variability on the timescale of years to centuries. To this end, we have presented power spectral densities for both local and global surface air temperature from

simulation and observation-based data of the last millennia. On this basis, we concluded that locally there is a stronger scaling and increased variance in reconstructions as compared to simulations. Using statistical analysis, we found that local temperature series extracted from simulations and paleoclimate reconstructions show different scaling behavior, with proxy records hinting at a stronger persistence. Furthermore, we have largely extended the spectral analysis of climatic drivers by estimating the joint PSD from CO₂, solar, volcanic, and orbital forcing using Monte Carlo simulation. Hereby, we discovered a scale break at the period of approximately 7 yr. Moreover, we have presented the spectral gain, describing the timescale-dependent forced temperature response. We found that it is mostly consistent across data sets and indicates an increasing internal variability on timescales of decades to centuries.

Our analysis of the spectral gain was limited to global average values and those timescales where linearity can be reasonably assumed [42, 43, 110]. Nonlinearities are inherent to the climate system, for example, due to the temperature-albedo feedback. Thus, it will be necessary to examine their possible effects on multiple spatiotemporal scales to further extend this work. Studying nonlinearities could also shine new light on the mechanisms of scaling in Earth’s climate, which are not yet fully understood and might be linked to nonlinearities as well [6]. Furthermore, we have focused on the current interglacial, the Holocene. This is because climate variability has been demonstrated to depend on the mean climate state [82]. Furthermore, major shifts in climate could potentially violate the basic assumption of weak stationarity for spectral analysis. Thus, the conclusions laid out here cannot be readily applied to other climate states, such as glacial periods, which is an issue for future studies. Clearly, understanding the dependence of temperature variability on global warming demands additional work.

Ideally, our findings should be replicated by employing models with increased internal variability on longer timescales and paleoclimate data that provides improved spatiotemporal resolution. In particular, investigating the relationship between spatial and temporal disagreement is a key task for future analyses. Optimized analysis of noise sources and spectral analysis of (pseudo-)proxy records could help to expand the data basis of proxy records with decadal resolution [59, 111, 112]. Regarding climate models, an improved representation of processes that increase Earth’s long-term memory, such as an interactive carbon cycle and dynamical ice sheets, might strengthen the long-range dependence and persistence of surface air temperature. A better understanding of unforced low-frequency oscillations as well as abrupt changes will be necessary to improve the representation of local fluctuations and could further help to understand nonlinear feedback and possible bifurcations in the climate system. Future studies could also continue to explore how internally generated and externally forced vari-

ability compares on different spatial scales. Research on the interrelation between internal and forced changes, as well as local, regional, and global variability, might prove important and could be conducted using single-forcing experiments from ensembles of model simulations.

Managing climate risks requires a detailed understanding of temperature variability. Locally and on timescales between years and centuries, there is an urgency to address discrepancies to make further progress in climate modeling. In this study, we have singled out the key characteristics of temperature variability and showed that the timescale dependency of local temperature variations from observation-based data and model simulations differs. Our results have demonstrated that the scaling behavior and spectral gain are easy-to-use yet effective and promising tools for investigating variability in Earth’s dynamic climate.

Code to reproduce all figures is available at [113].

ACKNOWLEDGMENTS

This manuscript is based upon data provided by the World Climate Research Programme’s Working Group on Coupled Modelling, which is responsible for CMIP and PMIP. We thank the research groups listed in Tables S1 and S2 for producing and making available their data from model outputs, measurements, paleoclimate, and forcing reconstructions. This study benefited from discussions within the CVAS working group, a working group of the Past Global Changes (PAGES) project. We thank T. Gasenzer, T. Kunz, and N. Weitzel for discussions and J. Bühler, M. Casado, M. Schillinger, and E. Ziegler for helpful comments on the manuscript. We are grateful to Aimé Fournier and one anonymous referee for their constructive and valuable review. This research has been funded by the Heidelberg Graduate School for Physics, by the PalMod project (subproject no. 01LP1926C), and by the Deutsche Forschungsgemeinschaft (DFG, German Research Foundation) – project no. 395588486.

Appendix A: Relation between power spectral density and variance

The power spectral density of a weakly-stationary, stochastic process is given by the Fourier transform of the autocorrelation $S(f) = \mathcal{F}\{R(h)\}$ with frequency f and lag $h = t_2 - t_1$ between two points in time [19, 20]. For zero lag and zero mean, the integral of the PSD corresponds to the variance of the signal [80]. Instead of frequency, we use the period $\tau = 1/f$ to express the PSD and spectral gain. The integration of expression (1) is divergent for $\beta < 1$ and $f \rightarrow \infty$ which requires a high-frequency cut-off, such as described by Lovejoy *et al.* [38]. In case of temperature time series considered here, this

is naturally defined by the temporal resolution, setting the maximum frequency.

Appendix B: Autocovariance of long-range memory processes

Fractional Brownian motion (fBm) and fractional Gaussian noise (fGn) are fully described by their correlation properties [30, 114], summarized below. The autocovariance function of fBm $B(t)$ reads

$$\begin{aligned}\gamma(t', t) &= \langle B(t')B(t) \rangle = \frac{V_\beta}{2} (|t|^{\beta-1} + |t'|^{\beta-1} - |t' - t|^{\beta-1}) \\ &\propto 1 + \left| \frac{t'}{t} \right|^{\beta-1} - \left| 1 - \frac{t'}{t} \right|^{\beta-1} \quad (\text{B1})\end{aligned}$$

for $1 < \beta < 3$. V_β is a positive constant factor related to $\langle (B(t') - B(t))^2 \rangle = V_\beta |t' - t|^{\beta-1}$. By definition, fGn is the series of stationary increments $B(t') - B(t)$ and shows spectral exponent $-1 < \beta' = \beta - 2 < 1$ for $f \ll 1/\pi\Delta t$ with $\Delta t = t' - t$. Its autocovariance

$$\begin{aligned}\gamma(h) &= \langle (B(t+1+h) - B(t+h))(B(t+1) - B(t)) \rangle \\ &= \frac{V_\beta}{2} |h-1|^{\beta'+1} - 2|h|^{\beta'+1} + |h+1|^{\beta'+1}, \quad (\text{B2})\end{aligned}$$

depends only on the lag $h \in \mathbb{Z}$, where we set $\Delta t = 1$ without loss of generality. The fGn has a power spectrum of the form [115]

$$S(f) \propto \frac{\sin^2(\pi\Delta t f)}{2\pi\Delta t f^{|\beta'+2|}}, \quad (\text{B3})$$

with the slowly varying factor

$$\sin^2(\pi\Delta t f) \xrightarrow{f/f_{\max} \rightarrow 0} (\pi\Delta t)^2 f^2, \quad f_{\max} = 1/\pi\Delta t. \quad (\text{B4})$$

Considering positive frequencies $f > 0$, the spectrum (B3) can be approximated by the power law $S(f) \sim 1/f^{\beta'}$ if $f \ll f_{\max}$. For $f \gtrsim f_{\max}$, however, the fGn has a similar spectral shape to fBm [114]. We account for this by considering sufficiently long periods. To give an example, $10^{0.58} \text{ yr}^{-1} \lesssim f_{\max} \lesssim 10^{2.7} \text{ yr}^{-1}$ corresponds to $6 \text{ h} \lesssim \Delta t \lesssim 1 \text{ mon}$.

For all $|t'/t| \gg 1$, the covariances (B1) keep growing for $\beta > 2$ (persistence) and stay bounded for $\beta < 2$ (antipersistence). As a result, equation (B1) involves “nonlinear pseudo-trends” [30] for $B(t')$ conditioned on $B(t)$, which diverge for $\beta > 2$ and converge for $\beta < 2$. According to Eq. (B2), fGn is persistent for $\beta' > 0$ and antipersistent for $\beta' < 0$. Ordinary Brownian motion corresponds to $\beta = 2$ and white noise to $\beta' = 0$. The sequence of partial sums of the autocovariance function diverges for fGn with $\beta' > 0$ and fBm with $\beta > 2$. The process is nonsummable and said to possess long-range memory.

Appendix C: Spectral gain for linear systems

In a time-invariant linear system, the output

$$y(t) = \int_{-\infty}^{\infty} h(u)x(t-u)du \quad (\text{C1})$$

is given by the input time series $x(t)$ and the impulse response function $h(u)$ [80]. The Fourier transform $H(f) = \mathcal{F}\{h(u)\} = G(f)e^{i\phi(f)}$ gives the frequency response function, also called the transfer function. $G(f)$ and $\phi(f)$ are the gain and phase, respectively. The integral (C1) corresponds to a product in frequency space $\mathcal{F}\{y(t)\} = H(f)\mathcal{F}\{x(t)\}$. This relates the PSD of the output $S_y(f)$ to the one of the input $S_x(f)$ via

$$S_y(f) = |H(f)|^2 S_x(f) = G^2(f) S_x(f). \quad (\text{C2})$$

Appendix D: Analytical solution to the PSD of intermittent volcanic forcing

We investigate the power spectral density of intermittent volcanic forcing by approximating the eruption time series in a simplified way as a stochastic signal $X(t) = \delta(t - t_i)$. This function is zero at all times except t_i , when an event of unique amplitude occurs. We denote $T_i = t_i - t_{i-1}$ the time intervals between two events. We use the fact that the PSD cannot be calculated only from the covariance, but also from the Laplace transform $S(X, f) = 2 \lim_{\epsilon \rightarrow 0} \langle |\mathcal{L}(X(t), \frac{\epsilon}{2} - 2\pi i f)|^2 \rangle$ [116]. Based on this approach, the power spectral density

$$S(f) = \mu_T \frac{1 - |\rho(f)|^2}{|1 - \rho(f)|^2}, \quad f > 0 \quad (\text{D1})$$

becomes a function of the Fourier transform of the probability density function $\rho(f) = \mathcal{F}\{\rho(T)\}$ and the inverse mean interval between two events $\mu_T = \langle T \rangle^{-1}$ [116, 117]. An exponentially decaying probability distribution $\rho(T) = \mu_T \exp(-\mu_T T) \Theta(T)$ for volcanic forcing is suggested [118], and we have checked this for the data sets considered. The Fourier transform reads $\rho(f) = \mu_T (\mu_T + 2\pi i f)^{-1}$ such that $1 - |\rho(f)|^2 = |1 - \rho(f)|^2$. As a consequence, the PSD (D1) takes a constant value. We can observe this white noise behavior in Fig. 5 and 6 (a) on timescales longer than a few years, which is on the order of characteristic return times for eruptions. Below these timescales, the variability considerably drops. This analytical result provides an independent verification of the PSD for volcanic forcing and its scale break.

Appendix E: Monte Carlo sampling of the spectral gain

We simulate the spectral gain (4), as well as the PSD of global mean temperature and the joint PSD of radiative forcing using a Monte Carlo approach with $N = 1000$

realizations to account for sampling biases. The PSD of global mean temperature is sampled for three groups: the observation-based data, the model simulations from group M_0 , and those from M_0 together with M_+ (Table S1 [47]). Here, only models from the groups M_0 and M_+ are considered to exclude model artifacts and to represent the historical temperature response in the best possible way.

We sample the simulation-based PSD from the average PSD of the simulations using uniformly distributed random weights. To obtain the observation-based PSD, we use the global mean temperature from HadCRUT4, ERA5, and a 7000-member reconstruction ensemble provided by PAGES2k [46]. This ensemble allows us to sample the PSD by randomly selecting one ensemble member and form the mean of its spectrum with that of the ERA5 and HadCRUT4 temperature. The joint PSD of radiative forcing is calculated from all forcing reconstructions considered in this work except the Fröhlich *et al.* solar forcing, which has too low temporal resolution above

interannual scales (Table S3 and Fig. S5 [47]). We assume the PSD of CO_2 and orbital forcing as fixed since its spectral power is comparatively low on multi-decadal scales. We sample the PSD of solar forcing by using uniformly distributed weights when forming the average PSD of all solar reconstructions. Similarly, the PSD of volcanic forcing is obtained. In addition, we randomly vary the conversion factor between $(-18)^{-1}$ and $(-25)^{-1} \text{ Wm}^{-2}/\text{AOD}$ [78]. The joint PSD of radiative forcing is calculated by linear summation of the PSD from CO_2 , orbital, solar, and volcanic forcing.

Using this sampling scheme, our Monte Carlo produces two outcomes: First, we compute the PSD of global mean temperature and the joint PSD of radiative forcing by simulating an ensemble of N realizations for both forcing and response. Second, we sample the spectral gain directly from the quotient (4) in each of the N realizations. In both cases, the average of the generated N -member ensemble and its 5% and 95% quantiles constitute the result of our Monte Carlo simulation.

-
- [1] J. Bjerknes, A possible response of the atmospheric Hadley circulation to equatorial anomalies of ocean temperature, *Tellus* **18**, 820 (1966).
 - [2] S. Arrhenius, XXXI. On the influence of carbonic acid in the air upon the temperature of the ground, *The London, Edinburgh, and Dublin Philosophical Magazine and Journal of Science* **41**, 237 (1896).
 - [3] J. B. J. Fourier, Remarques générales sur les températures du globe terrestre et des espaces planétaires, *Annales de Chimie et de Physique*, 136 (1824).
 - [4] R. W. Katz and B. G. Brown, Extreme events in a changing climate: Variability is more important than averages, *Climatic Change* **21**, 289 (1992).
 - [5] M. Ghil and V. Lucarini, The physics of climate variability and climate change, *Reviews of Modern Physics* **92**, 10.1103/RevModPhys.92.035002 (2020).
 - [6] C. L. E. Franzke et al., The Structure of Climate Variability Across Scales, *Reviews of Geophysics* 10.1029/2019RG000657 (2020).
 - [7] J. E. Tierney et al., Past climates inform our future, *Science* **370**, 10.1126/science.aay3701 (2020).
 - [8] T. Laepple and P. Huybers, Global and regional variability in marine surface temperatures, *Geophysical Research Letters* 10.1002/2014GL059345 (2014).
 - [9] T. Laepple and P. Huybers, Ocean surface temperature variability: Large model-data differences at decadal and longer periods, *Proceedings of the National Academy of Sciences of the United States of America* **111**, 16682 (2014).
 - [10] L. A. Parsons, G. R. Loope, J. T. Overpeck, T. R. Ault, R. Stouffer, and J. E. Cole, Temperature and precipitation variance in CMIP5 simulations and paleoclimate records of the last millennium, *Journal of Climate* 10.1175/JCLI-D-16-0863.1 (2017).
 - [11] F. C. Ljungqvist, Q. Zhang, G. Brattström, P. J. Krusic, A. Seim, Q. Li, Q. Zhang, and A. Moberg, Centennial Scale Temperature Change in Last Millennium Simulations and Proxy-Based Reconstructions, *Journal of Climate* **32**, 2441 (2019).
 - [12] J. C. Bühler, C. Roesch, M. Kirschner, L. Sime, M. D. Holloway, and K. Rehfeld, Comparison of the oxygen isotope signatures in speleothem records and ihadcm3 model simulations for the last millennium, *Climate of the Past* **17**, 985 (2021).
 - [13] W. B. Anderson, R. Seager, W. Baethgen, M. Cane, and L. You, Synchronous crop failures and climate-forced production variability, *Science Advances* **5**, 10.1126/sciadv.aaw1976 (2019).
 - [14] M. Crucifix, A. D. Vernal, and C. Franzke, Centennial To Millennial Climate Variability, *Past Global Changes Mag.* **25**, doi:10.22498/pages.25.3 (2017).
 - [15] M. Rypdal, H. B. Fredriksen, E. Myrvoll-Nilsen, K. Rypdal, and S. H. Sørbye, Emergent scale invariance and climate sensitivity, *Climate* **6**, 1 (2018).
 - [16] C. L. E. Franzke and T. J. O’Kane, eds., *Nonlinear and Stochastic Climate Dynamics* (Cambridge University Press, Cambridge, 2017).
 - [17] T. P. Barnett et al., Detection and attribution of recent climate change: A status report, *Bulletin of the American Meteorological Society* **80**, 10.1175/1520-0477(1999)080<2631:DAAORC>2.0.CO;2 (1999).
 - [18] N. Bindoff et al., Detection and attribution of climate change: From global to regional, in *Climate Change 2013: The Physical Science Basis. Contribution of Working Group I to the Fifth Assessment Report of the Intergovernmental Panel on Climate Change*, edited by I. P. o. C. Change (Cambridge University Press, 2013).
 - [19] N. Wiener, Generalized harmonic analysis, *Acta Mathematica* **55**, 117 (1930).
 - [20] A. Khintchine, Korrelationstheorie der stationären stochastischen Prozesse, *Mathematische Annalen* **109**, 604 (1934).
 - [21] C. Wunsch, The spectral description of climate change

- including the 100 ky energy, *Climate Dynamics* **20**, 353 (2003).
- [22] C. Franzke, Nonlinear trends, long-range dependence, and climate noise properties of surface temperature, *Journal of Climate* 10.1175/JCLI-D-11-00293.1 (2012).
- [23] P. Huybers and W. Curry, Links between annual, Milankovitch and continuum temperature variability, *Nature* **441**, 329 (2006).
- [24] S. Lovejoy, A voyage through scales, a missing quadrillion and why the climate is not what you expect, *Climate Dynamics* **44**, 3187 (2015).
- [25] T. Nilsen, K. Rypdal, and H. B. Fredriksen, Are there multiple scaling regimes in Holocene temperature records?, *Earth System Dynamics* **7**, 419 (2016).
- [26] H. B. Fredriksen and M. Rypdal, Long-range persistence in global surface temperatures explained by linear multibox energy balance models, *Journal of Climate* 10.1175/JCLI-D-16-0877.1 (2017).
- [27] K. Fraedrich, U. Luksch, and R. Blender, $1/f$ -model for long-time memory of the ocean surface temperature, *Physical Review E* **70**, 037301 (2004).
- [28] K. Rypdal, L. Østvand, and M. Rypdal, Long-range memory in Earth’s surface temperature on time scales from months to centuries, *Journal of Geophysical Research: Atmospheres* **118**, 7046 (2013).
- [29] F. Zhu, J. Emile-Geay, N. P. McKay, G. J. Hakim, D. Khider, T. R. Ault, E. J. Steig, S. Dee, and J. W. Kirchner, Climate models can correctly simulate the continuum of global-average temperature variability, *Proceedings of the National Academy of Sciences of the United States of America* **116**, 8728 (2019).
- [30] B. B. Mandelbrot and J. W. Van Ness, Fractional Brownian Motions, Fractional Noises and Applications, *SIAM Review* **10**, 10.1137/1010093 (1968).
- [31] B. D. Malamud and D. L. Turcotte, Self-affine time series: measures of weak and strong persistence, *J. Stat. Plan. Infer.* **80**, 173 (1999).
- [32] J. P. Peixoto and A. H. Oort, Physics of climate, *Reviews of Modern Physics* **56**, 365 (1984).
- [33] E. J. Rohling et al., Making sense of palaeoclimate sensitivity, *Nature* **491**, 683 (2012).
- [34] E. J. Rohling, G. Marino, G. L. Foster, P. A. Goodwin, A. S. von der Heydt, and P. Köhler, Comparing Climate Sensitivity, Past and Present, *Annual Review of Marine Science* **10**, 261 (2018).
- [35] F. Zhang, Y. Qiang Sun, L. Magnusson, R. Buizza, S. J. Lin, J. H. Chen, and K. Emanuel, What is the predictability limit of midlatitude weather?, *Journal of the Atmospheric Sciences* 10.1175/JAS-D-18-0269.1 (2019).
- [36] J. D. Pelletier, Natural variability of atmospheric temperatures and geomagnetic intensity over a wide range of time scales, *Proceedings of the National Academy of Sciences of the United States of America* **99**, 2546 (2002).
- [37] J. Lohmann and P. D. Ditlevsen, Random and externally controlled occurrences of Dansgaard–Oeschger events, *Climate of the Past* **14**, 609 (2018).
- [38] S. Lovejoy and F. Lambert, Spiky fluctuations and scaling in high-resolution epica ice core dust fluxes, *Climate of the Past* **15**, 1999 (2019).
- [39] K. Marvel, G. A. Schmidt, R. L. Miller, and L. S. Nazarenko, Implications for climate sensitivity from the response to individual forcings, *Nature Climate Change* **6**, 386 (2016).
- [40] A. P. Schurer, G. C. Hegerl, M. E. Mann, S. F. B. Tett, and S. J. Phipps, Separating Forced from Chaotic Climate Variability over the Past Millennium, *Journal of Climate* **26**, 6954 (2013).
- [41] S. Lovejoy and D. Schertzer, Stochastic and scaling climate sensitivities: Solar, volcanic and orbital forcings, *Geophysical Research Letters* **39**, <https://doi.org/10.1029/2012GL051871> (2012).
- [42] S. Lovejoy and C. Varotsos, Scaling regimes and linear/nonlinear responses of last millennium climate to volcanic and solar forcings, *Earth System Dynamics* 10.5194/esd-7-133-2016 (2016).
- [43] K. Rypdal and M. Rypdal, Comment on “Scaling regimes and linear/nonlinear responses of last millennium climate to volcanic and solar forcing” by S. Lovejoy and C. Varotsos (2016), *Earth System Dynamics* **7**, 597 (2016).
- [44] J. Mitchell, An overview of climatic variability and its causal mechanisms, *Quaternary Research* **6**, 481 (1976).
- [45] A. Henderson-Sellers and K. McGuffie, *A Climate Modelling Primer* (Wiley, Chichester, UK, 1987).
- [46] PAGES 2k Consortium., Consistent multidecadal variability in global temperature reconstructions and simulations over the Common Era, *Nature Geoscience* **12**, 643 (2019).
- [47] See the Supplemental Material for further information on data sets and benchmarks.
- [48] B. L. Otto-Bliesner, E. C. Brady, J. Fasullo, A. Jahn, L. Landrum, S. Stevenson, N. Rosenbloom, A. Mai, and G. Strand, Climate variability and change since 850 CE an ensemble approach with the Community Earth System Model, *Bulletin of the American Meteorological Society* 10.1175/BAMS-D-14-00233.1 (2016).
- [49] J. H. Jungclaus et al., Climate and carbon-cycle variability over the last millennium, *Climate of the Past* 10.5194/cp-6-723-2010 (2010).
- [50] Y. Zhong, A. Jahn, G. H. Miller, and A. Geirsdottir, Asymmetric Cooling of the Atlantic and Pacific Arctic During the Past Two Millennia: A Dual Observation-Modeling Study, *Geophysical Research Letters* **45**, 12,412 (2018).
- [51] P. Braconnot, D. Zhu, O. Marti, and J. Servonnat, Strengths and challenges for transient Mid- to Late Holocene simulations with dynamical vegetation, *Climate of the Past* **15**, 997 (2019).
- [52] N. Fischer and J. H. Jungclaus, Evolution of the seasonal temperature cycle in a transient Holocene simulation: Orbital forcing and sea-ice, *Climate of the Past* 10.5194/cp-7-1139-2011 (2011).
- [53] Z. Liu, Transient simulation of last deglaciation with a new mechanism for Bølling–Allerød warming, *Science* **325**, 10.1126/science.1171041 (2009).
- [54] C. P. Morice, J. J. Kennedy, N. A. Rayner, and P. D. Jones, Quantifying uncertainties in global and regional temperature change using an ensemble of observational estimates: The HadCRUT4 data set, *Journal of Geophysical Research Atmospheres* **117**, 10.1029/2011JD017187 (2012).
- [55] H. Hersbach, B. Bell, P. Berrisford, and S. Hirahara, The ERA5 global reanalysis, *Quarterly Journal of the Royal Meteorological Society*, 1999 (2020).
- [56] PAGES2k Consortium., A global multiproxy database for temperature reconstructions of the Common Era, *Scientific Data* 10.1038/sdata.2017.88 (2017).

- [57] J. W. Kantelhardt, Fractal and multifractal time series, in *Mathematics of Complexity and Dynamical Systems*, edited by R. A. Meyers (Springer, New York, 2011) pp. 463–487.
- [58] T. Laepple, T. Münch, M. Casado, M. Hoerhold, A. Landais, and S. Kipfstuhl, On the similarity and apparent cycles of isotopic variations in East Antarctic snow pits, *Cryosphere* 10.5194/tc-12-169-2018 (2018).
- [59] M. Casado, T. Münch, and T. Laepple, Climatic information archived in ice cores: impact of intermittency and diffusion on the recorded isotopic signal in Antarctica, *Climate of the Past* **16**, 1581 (2020).
- [60] T. J. Crowley, Causes of climate change over the past 1000 years, *Science* 10.1126/science.289.5477.270 (2000).
- [61] G. C. Hegerl, T. J. Crowley, M. Allen, W. T. Hyde, H. N. Pollack, J. Smerdon, and E. Zorita, Detection of Human Influence on a New, Validated 1500-Year Temperature Reconstruction, *Journal of Climate* **20**, 650 (2007).
- [62] P. Braconnot, S. P. Harrison, M. Kageyama, P. J. Bartlein, V. Masson-Delmotte, A. Abe-Ouchi, B. Otto-Bliesner, and Y. Zhao, Evaluation of climate models using palaeoclimatic data, *Nature Climate Change* **2**, 417 (2012).
- [63] G. A. Schmidt et al., Climate forcing reconstructions for use in PMIP simulations of the Last Millennium (v1.1), *Geoscientific Model Development* **5**, 185 (2012).
- [64] G. Delaygue and E. Bard, An Antarctic view of Beryllium-10 and solar activity for the past millennium, *Climate Dynamics* **36**, 2201 (2011).
- [65] F. Steinhilber, J. Beer, and C. Fröhlich, Total solar irradiance during the Holocene, *Geophysical Research Letters* **36**, 10.1029/2009GL040142 (2009).
- [66] Y. Wang, J. L. Lean, and N. R. Sheeley, Jr., Modeling the Sun’s Magnetic Field and Irradiance since 1713, *The Astrophysical Journal* 10.1086/429689 (2005).
- [67] R. Muscheler, F. Joos, J. Beer, S. A. Müller, M. Vonmoos, and I. Snowball, Solar activity during the last 1000yr inferred from radionuclide records, *Quaternary Science Reviews* **26**, 82 (2007).
- [68] L. E. Vieira and S. K. Solanki, Evolution of the solar magnetic flux on time scales of years to millenia, *Astronomy and Astrophysics* 10.1051/0004-6361/200913276 (2010).
- [69] C. Gao, A. Robock, and C. Ammann, Volcanic forcing of climate over the past 1500 years: An improved ice core-based index for climate models, *Journal of Geophysical Research: Atmospheres* **113**, 10.1029/2008JD010239 (2008).
- [70] A. L. Berger, Long-term variations of daily insolation and Quaternary climatic changes., *Journal of Atmospheric Sciences* 10.1175/1520-0469(1978)035<2362:ltvodi>2.0.co;2 (1978).
- [71] M. Crucifix, Palinsol - Package (R) (2016).
- [72] M. Toohey and M. Sigl, Reconstructed volcanic stratospheric sulfur injections and aerosol optical depth, 500 BCE to 1900 CE, version 2, World Data Center for Climate (WDCC) at DKRZ 10.1594/WDCC/eVolv2k.v2 (2017).
- [73] C. Fröhlich, Solar irradiance variability since 1978: Revision of the PMOD composite during solar cycle 21, *Space Science Reviews* **125**, 53 (2006).
- [74] C. D. Keeling, R. B. Bacastow, A. E. Bainbridge, C. A. Ekdahl Jr., P. R. Guenther, L. S. Waterman, and J. F. S. Chin, Atmospheric carbon dioxide variations at mauna loa observatory, hawaii, *Tellus* **28**, 538 (1976).
- [75] J. Pongratz, C. Reick, T. Raddatz, and M. Claussen, A reconstruction of global agricultural areas and land cover for the last millennium, *Global Biogeochemical Cycles* **22**, 10.1029/2007GB003153 (2008).
- [76] G. Myhre, E. J. Highwood, K. P. Shine, and F. Stordal, New estimates of radiative forcing due to well mixed greenhouse gases, *Geophysical Research Letters* **25**, 2715 (1998).
- [77] G. A. Schmidt et al., Climate forcing reconstructions for use in PMIP simulations of the last millennium (v1.0), *Geoscientific Model Development* **4**, 33 (2011).
- [78] G. Myhre et al., Anthropogenic and natural radiative forcing supplementary material., in *Climate Change 2013: The Physical Science Basis. Contribution of Working Group I to the Fifth Assessment Report of the Intergovernmental Panel on Climate Change*, edited by Intergovernmental Panel on Climate Change (Cambridge University Press, Cambridge, 2014) pp. 1–30.
- [79] T. Laepple and P. Huybers, Reconciling discrepancies between Uk37 and Mg/Ca reconstructions of Holocene marine temperature variability, *Earth and Planetary Science Letters* **375**, 418 (2013).
- [80] C. Chatfield and H. Xing, *The Analysis of Time Series: An Introduction with R*, 7th ed., Chapman & Hall / CRC Texts in Statistical Science (CRC Press, 2019).
- [81] H. B. Fredriksen and K. Rypdal, Spectral characteristics of instrumental and climate model surface temperatures, *Journal of Climate* **29**, 1253 (2016).
- [82] K. Rehfeld, T. Münch, S. L. Ho, and T. Laepple, Global patterns of declining temperature variability from the Last Glacial Maximum to the Holocene, *Nature* **554**, 356 (2018).
- [83] D. B. Percival and A. T. Walden, *Spectral Analysis for Physical Applications: Multitaper and Conventional Univariate Techniques* (Cambridge University Press, Cambridge, UK, 1993).
- [84] P. Yiou, E. Baert, and M. F. Loutre, Spectral analysis of climate data, *Surveys in Geophysics* **17**, 619 (1996).
- [85] J. W. Kirchner, Aliasing in $1/f^\alpha$ noise spectra: Origins, consequences, and remedies, *Phys. Rev. E* **71**, 66110 (2005).
- [86] L. Østvand, T. Nilsen, K. Rypdal, D. Divine, and M. Rypdal, Long-range memory in internal and forced dynamics of millennium-long climate model simulations, *Earth System Dynamics* **5**, 295 (2014).
- [87] J. L. Fleiss and J. Cohen, The Equivalence of Weighted Kappa and the Intraclass Correlation Coefficient as Measures of Reliability, *Educational and Psychological Measurement* **33**, 613 (1973).
- [88] O. Geoffroy, D. Saint-Martin, D. J. Olivié, A. Voldoire, G. Bellon, and S. Tytéca, Transient climate response in a two-layer energy-balance model. Part I: Analytical solution and parameter calibration using CMIP5 AOGCM experiments, *Journal of Climate* **26**, 1841 (2013).
- [89] D. G. MacMynowski, H.-J. Shin, and K. Caldeira, The frequency response of temperature and precipitation in a climate model, *Geophysical Research Letters* **38**, <https://doi.org/10.1029/2011GL048623> (2011).
- [90] A. Kirkevåg, T. Iversen, J. E. Kristjánsson, Ø. Seland, and J. B. Debernard, On the additivity of climate response to anthropogenic aerosols and CO₂, and the en-

- hancement of future global warming by carbonaceous aerosols, *Tellus, Series A: Dynamic Meteorology and Oceanography* **60 A**, 10.1111/j.1600-0870.2008.00308.x (2008).
- [91] H. Shiogama, D. A. Stone, T. Nagashima, T. Nozawa, and S. Emori, On the linear additivity of climate forcing-response relationships at global and continental scales, *International Journal of Climatology* **33**, 10.1002/joc.3607 (2013).
- [92] G. A. Meehl, W. M. Washington, C. M. Ammann, J. M. Arblaster, T. M. Wigley, and C. Tebaldi, Combinations of natural and anthropogenic forcings in twentieth-century climate, *Journal of Climate* **17**, 10.1175/1520-0442(2004)017<3721:CONAAF>2.0.CO;2 (2004).
- [93] V. Ramaswamy and C. T. Chen, Linear additivity of climate response for combined albedo and greenhouse perturbations, *Geophysical Research Letters* **24**, 10.1029/97GL00248 (1997).
- [94] J. Jungclaus, private communication (2020).
- [95] G. Danabasoglu, On Multidecadal Variability of the Atlantic Meridional Overturning Circulation in the Community Climate System Model Version 3, *Journal of Climate* **21**, 5524 (2008).
- [96] T. Kunz and T. Laepple, Frequency-dependent estimation of effective spatial degrees of freedom, *Journal of Climate* **34**, 10.1175/JCLI-D-20-0228.1 (2021).
- [97] T. Kunz and T. Laepple, Time-scale dependent estimation of spatial degrees of freedom, in *EGU General Assembly Conference Abstracts*, EGU General Assembly Conference Abstracts (2018) p. 17995.
- [98] S.-W. Yeh, J.-S. Kug, B. Dewitte, M.-H. Kwon, B. P. Kirtman, and F.-F. Jin, El Niño in a changing climate, *Nature* **461**, 511 (2009).
- [99] M. Reschke, K. Rehfeld, and T. Laepple, Empirical estimate of the signal content of Holocene temperature proxy records, *Climate of the Past* **15**, 521 (2019).
- [100] L. J. Lücke, G. C. Hegerl, A. P. Schurer, and R. Wilson, Effects of memory biases on variability of temperature reconstructions, *Journal of Climate* **32**, 10.1175/JCLI-D-19-0184.1 (2019).
- [101] J. L. Fleiss, B. Levin, and M. C. Paik, *Statistical Methods for Rates and Proportions*, 3rd ed., Wiley Series in Probability and Statistics (Wiley, 2013).
- [102] A. Clauset, C. R. Shalizi, and M. E. J. Newman, Power-law distributions in empirical data, *SIAM Review* **51**, 661–703 (2009).
- [103] B. P. Kirtman et al., Impact of ocean model resolution on CCSM climate simulations, *Climate Dynamics* **39**, 1303 (2012).
- [104] J. M. Klavans, A. Poppick, S. Sun, and E. J. Moyer, The influence of model resolution on temperature variability, *Climate Dynamics* **48**, 3035 (2017).
- [105] D. L. Hodson and R. T. Sutton, The impact of resolution on the adjustment and decadal variability of the Atlantic meridional overturning circulation in a coupled climate model, *Climate Dynamics* **39**, 10.1007/s00382-012-1309-0 (2012).
- [106] L. J. Gray et al., Solar influences on climate, *Reviews of Geophysics* **48**, 10.1029/2009RG000282 (2010).
- [107] E. Hertwig, F. Lunkeit, and K. Fraedrich, Low-frequency climate variability of an aquaplanet, *Theoretical and Applied Climatology* **121**, 459 (2015).
- [108] W. R. Peltier and G. Vettoretti, Dansgaard-Oeschger oscillations predicted in a comprehensive model of glacial climate: A “kicked” salt oscillator in the Atlantic, *Geophysical Research Letters* **41**, 7306 (2014).
- [109] M. Klockmann, U. Mikolajewicz, H. Kleppin, and J. Marotzke, Coupling of the Subpolar Gyre and the Overturning Circulation During Abrupt Glacial Climate Transitions, *Geophysical Research Letters* **47**, 10.1029/2020GL090361 (2020).
- [110] L. Fernández-Donado, J. González-Rouco, C. Raible, C. Ammann, D. Barriopedro, E. García-Bustamante, J. H. Jungclaus, S. Lorenz, J. Luterbacher, S. J. Phipps, et al., Large-scale temperature response to external forcing in simulations and reconstructions of the last millennium, *Climate of the Past* **9**, 393 (2013).
- [111] T. Kunz, A. M. Dolman, and T. Laepple, A spectral approach to estimating the timescale-dependent uncertainty of paleoclimate records – Part 1: Theoretical concept, *Climate of the Past* **16**, 1469 (2020).
- [112] A. M. Dolman, T. Kunz, J. Groeneveld, and T. Laepple, A spectral approach to estimating the timescale-dependent uncertainty of paleoclimate records – part 2: Application and interpretation, *Climate of the Past* **17**, 825 (2021).
- [113] <https://github.com/paleovar/timescaledependency>.
- [114] A. Fournier, private communication (2021).
- [115] S. Mallat, Chapter 6 - wavelet zoom, in *A Wavelet Tour of Signal Processing* (Academic Press, Boston, 2009) 3rd ed., pp. 205–261.
- [116] R. L. Stratonovich, *Topics in the Theory of Random Noise* (Gordon and Breach, New York, 1967).
- [117] B. Lindner, Superposition of many independent spike trains is generally not a poisson process, *Phys. Rev. E* **73**, 022901 (2006).
- [118] P. Papale, Global time-size distribution of volcanic eruptions on Earth, *Scientific Reports* **8**, 6838 (2018).

Supplemental Material for
*Probing the timescale dependency of local and global variations
in surface air temperature from climate simulations and
reconstructions of the last millennia*

Beatrice Ellerhoff and Kira Rehfeld

LIST OF TABLES

I	Key specifications of model simulation and observation-based data	2
II	Key specification of climatic drivers	3
III	Key specification of paleoclimate data	4

LIST OF FIGURES

1	Global mean temperature over the Common Era	7
2	Climatic drivers over the last millennium	7
3	Temperature signals from proxy records over the last millennia	8
4	PSD of proxy records	9
5	Mean PSDs for radiative forcing reconstructions	10
6	PSD from last millennium runs and their PI control runs	10
7	Mean PSD from high- and low-frequency spectrum	11
8	Uncertainty quantification for irregularly sampled temperature proxies	11
9	The effect of sampling on the mean of local PSDs from proxy records	12
10	The effect of global warming on the spectral exponent β	12
11	Scaling of local temperature from simulation and proxies	13
12	Goodness of fit for local scaling coefficients from model simulations	14
13	PSD of disjoint time series of global mean temperature	15
14	Root-mean-squared error of LR and MLE	15
15	Comparison of LR and MLE for irregularly sampled data	16
16	Cross-correlations of the examined proxy records	17

TABLE I. Key specifications of model simulations and observation-based data used to estimate temperature variability. We give the main references (Doc.) of the simulation runs, observation-based data sets, and their forcing (Forc.). The groups M_+ and M_0 were assigned to better distinguish spectral properties when performing a Monte Carlo simulation of the spectral gain in the main manuscript. The temporal resolution Δt is given in months (m), hours (hr), years (yrs), and days. The spatial resolutions of atmosphere and ocean are denoted by the subscripts $^{\circ}\text{deg}_{at.}$ and $^{\circ}\text{deg}_{oc.}$, respectively.

Name	Doc.	Model	Δt	$^{\circ}\text{deg}_{at.}$	$^{\circ}\text{deg}_{oc.}$	Forc.	Time (CE)
Model simulations							
CESM 1 past2k ^a	[6]	CESM1	1 m	2	1	[7]	1-2005
CESM-LME 1 ^a	[8]	CESM1	1 m, 6 hr	2	1	[9]	850-2006
CESM-LME 1 cntl	[8]	CESM1	1 m	2	1	[9]	850-2006
MPI-M LM ^b	[10]	MPI-ESM	1 m, 6 hr	3.75	GR30 ^c	[10]	800-2005
MPI-M LM cntl	[10]	MPI-ESM	1 m	3.75	GR30 ^c	[10]	800-2005
HadCM3 LM1 ^a	[11]	iHadCM3	1 m	2.5 x 3.75	1.25	[12]	800-1850
IPSL-p6k ^a	[13]	IPSL-CM5A	2 m	2.5 x 1.27	2	[13]	4000 BCE - 2000
TraCE-21k	[14]	CCSM3	2 m	≈ 3.75	3.6 x v ^d	[15, 16]	4,000 BCE - 1990
TraCE-21k-ORB	[14]	CCSM3	10 yrs	≈ 3.75	3.6 x v ^d	[15, 16]	4,000 BCE - 1990
ECH5/MPIOM-p6k ^b	[17]	ECHAM5/MPI-OM	1 m	3.75	2	[15]	4000 BCE - 2000
Observation-based							
ERA5	[18]		1 m, 6 hr	2	2		1979-2019
HadCRUT4	[19]		7 days	5	5		1850-2019
PAGES2k	[3]		1 yr			[3]	0-2000

^a assigned to group M_0

^b assigned to M_+

^c curvilinear grid with nominal resolution of 3.0°

^d the latitudinal resolution is variable (v), with finer resolution near the equator ($\approx 0.90^{\circ}$)

TABLE II. Key specifications of climatic drivers used to estimate the power spectral density of radiative forcing as well as the gain function of the forced temperature response.

Name	Δt	Time (CE)
Volcanic forcing		
Crowley et al. ^a [21]	10 days	500BCE-1900
Gao et al. ^a [22]	1 yr	850-2000
Toohey et al. [23]		850-1850
Total solar irradiance		
Delaygue et al. ^{ab} [24]	1 yr	850-1850
Muscheler et al. ^{ab} [25]	1 yr	850-1850
Steinhilber et al. ^a [26]	1 yr	850-1850
Vieira et al. ^a [27, 28]	1 yr	850-1850
Wang et al. ^{ab} [29]	1 yr	1610-2009
Fröhlich et al. [30]	36 hr	1978-2017
CO₂		
Schmidt et al. ^a [20]	1 yr	850-2000
Keeling et al. [31]	1 hr	1970-2016
Insolation at 65°N		
Berger ^{ac} [15]	1 yr, 3 hr	0-2000

^a from the PMIP simulations of the Last Millennium [20]

^b when multiple versions were provided by PMIP, the “with-background”-version was considered here

^c computed with the **R**-package “Palinsol” [32]

TABLE III. Key specification of proxy records used to estimate local temperature variability. The first six columns (“ID” - “Proxy”) are taken from the PAGES2k database [3]. The ID is additionally marked with a start (★) in case the proxy record was used for calculating the agreement in scaling behavior between models and data. The cutoff identifies whether the proxy record was used for analyzing the potential impact of the recent global warming trend (Figure 6 and Figure 10). It indicates whether the necessary criteria for time series selection were fulfilled before 1850 (PI) and / or over the full historical (hist) period. Similarly, the selection column gives criteria for calculating the mean of local spectra and their comparison (Figure 6). The table spans multiple pages.

ID	Name	Lat	Lon	Elev.masl	Archive	Proxy	cutoff	selection
2	Africa-Lake Tanganyika.Tierney.2010	-6	28.5	28	lake sediment	TEX86	PI/hist	loose
3	Africa-Malawi.Powers.2011	-10	34.3	34	lake sediment	TEX86	PI/hist	loose
4	Africa-PI78-15.Tierney.2015	12	44.3	44	marine sediment	TEX86	PI/hist	strong/loose
39	Arc-BrayaSo.DAndrea.2011	67	-50.7	-51	lake sediment	alkenone	PI/hist	loose
40	Arc-Clegg2010	61.4	-143.6	-144	lake sediment	midge	PI/hist	loose
49*	Arc-GulfofAlaska.Wiles.2014	61	-146.6	-147	tree	TRW	PI/hist	strong/loose
50	Arc-HalletLake.McKay.2008	61.5	-146.2	-146	lake sediment	BSi	PI/hist	strong/loose
53	Arc-Iceland.Bergthorsson.1969	64.8	-18.4	-18	documents	historic	PI/hist	loose
56	Arc-Kongressvatn.DAndrea.2012	78	13.9	14	lake sediment	alkenone	PI/hist	loose
57	Arc-Lake4.Rolland.2009	65.1	-83.8	-84	lake sediment	chironomid	PI/hist	loose
59	Arc-LakeE.DAndrea.2011	67	-50.7	-51	lake sediment	alkenone	PI/hist	loose
60	Arc-LakePrieni-Ka.Luoto.2010	64.3	30.1	30	lake sediment	chironomid	PI/hist	loose
65	Arc-Luoto2009	60.3	25.4	25	lake sediment	midge	PI/hist	strong/loose
66	Arc-MackenzieDelta.Porter.2013	68.6	-133.9	-134	tree	missing	hist	strong/loose
69	Arc-MD992275.Jiang.2005	66.5	-17.7	-18	marine sediment	diatom	PI/hist	strong/loose
81	Arc-SoperLakeBaf.Hughen.2000	62.9	-69.9	-70	lake sediment	varve thickness	PI/hist	strong/loose
82*	Arc-StoreggaSlid.Sejrup.2011	63.8	5.3	5	marine sediment	foram d18O	PI/hist	strong/loose
83*	Arc-Thomas2008	69.9	-68.8	-69	lake sediment	varve thickness	PI/hist	strong/loose
85*	Arc-Tornetrask.Melvin.2013	68.3	19.6	20	tree	TRW	PI/hist	strong/loose
88*	Arc-Yamalia.Briffa.2013	66.8	68	68	tree	TRW	PI/hist	strong/loose
122	Asia-CentralChina.Wang.1998	29	113	113	documents	historic	PI/hist	strong/loose
130	Asia-Chu.2012.Sihailongwanlake	42.2	126.4	126	lake sediment	alkenone	PI/hist	strong/loose
151	Asia-EastChina.Wang.1990	30	117.5	118	documents	historic	PI/hist	strong/loose
152*	Asia-EastChinaereg.Wang.1998	34	120	120	documents	historic	PI/hist	strong/loose
157	Asia-FujianandTai.Wang.1998	24	121	121	documents	historic	PI/hist	strong/loose
167	Asia-Guangdong.Zheng.1982	23.2	113.2	113	documents	historic	PI/hist	strong/loose
168	Asia-Guangdong.Zhang.1980	23.5	112.5	112	documents	historic	PI/hist	strong/loose
182	Asia-Hunan.Jiangsu.Zhang.1980	28	116.5	116	documents	historic	PI/hist	strong/loose
205	Asia-KunashirIsland.Demezhko.2009	44	145.7	146	hybrid	hybrid	PI/hist	strong/loose
212	Asia-Lowerreaches.Zhang.1980	32.1	118.8	119	documents	historic	PI/hist	strong/loose
220	Asia-Middlereaches.Zhang.1980	30.5	114.5	114	documents	historic	PI/hist	strong/loose
273*	Asia-SO9039KGSOI.Munz.2015	24.8	65.9	66	marine sediment	foraminifera	PI/hist	strong/loose
275	Asia-SourthandMid.Demezhko.2007	55	59.5	60	borehole	borehole	PI/hist	loose

ID	Name	Lat	Lon	<i>Elev_masl</i>	Archive	Proxy	cutoff	selection
276	Asia-SouthChina.Wang.1998	23	114	114	documents	historic	PI/hist	strong/loose
331	Asia-ZhejiangandF.Zhang.1980	25	118	118	documents	historic	PI/hist	strong/loose
342*	Aus-MtRead.Cook.2006	-41.8	145.5	146	tree	TRW	PI/hist	strong/loose
343*	Aus-Oroko.Cook.2002	-43.2	170.3	170	tree	TRW	PI/hist	strong/loose
347	Eur-CentralandEa.Pla.2005	42.5	0.8	1	lake sediment	chrysophyte	PI/hist	loose
349	Eur-CentralEu.Dobrovlny.2010	49	13	13	documents	Documentary	PI/hist	strong/loose
350*	Eur-CoastofPortu.Abrantes.2011	41.1	-8.9	-9	marine sediment	alkenone	PI/hist	strong/loose
352*	Eur-FinnishLakes.Helama.2014	62	28.3	28	tree	MXD	PI/hist	strong/loose
354	Eur-LakeSilvapla.Larocque-Tobler.2010	46.5	9.8	10	lake sediment	chironomid	PI/hist	strong/loose
355*	Eur-LakeSilvapla.Trachsel.2010	46.5	9.8	10	lake sediment	reflectance	PI/hist	strong/loose
357*	Eur-NorthIceland.Ran.2011	66.5	-17.7	-18	marine sediment	diatom	PI/hist	strong/loose
359*	Eur-Seebergsee.Larocque-Tobler.2012	46.1	7.5	8	lake sediment	midge	PI/hist	strong/loose
364	Eur-Stockholm.Leijonhufvud.2010	59.3	18.1	18	documents	historic	PI/hist	strong/loose
365	Eur-Tallinn.Tarand.2001	59.4	24.8	25	documents	historic	PI/hist	strong/loose
391	NAm-BasinP	44.5	-70.1	-70	lake sediment	pollen	PI/hist	loose
450	NAm-ClearP	33.8	-79	-79	lake sediment	pollen	PI/hist	loose
457	NAm-ConroyL	46.3	-67.9	-68	lake sediment	pollen	PI/hist	loose
459	NAm-DarkL	45.3	-91.5	-92	lake sediment	pollen	PI/hist	loose
463	NAm-HellKt	46.2	-89.7	-90	lake sediment	pollen	PI/hist	loose
466*	NAm-LakeMina	45.9	-95.5	-96	lake sediment	pollen	PI/hist	strong/loose
467	NAm-LClouds	48	-91	-91	lake sediment	pollen	PI/hist	strong/loose
468	NAm-LittlePineL	45.3	-91.5	-92	lake sediment	pollen	PI/hist	loose
469*	NAm-LNoir	45.8	-75.1	-75	lake sediment	pollen	PI/hist	loose
485	NAm-RubyL	45.3	-91.5	-92	lake sediment	pollen	PI/hist	strong/loose
507	O2kLR-AlboranSea-TTR17-1384B.Nieto-Moreno.2012	36	-4.7	-5	marine sediment	alkenone	PI/hist	loose
508	O2kLR-AlboranSea-TTR17-1436B.Nieto-Moreno.2012	36.2	-4.3	-4	marine sediment	alkenone	PI/hist	loose
510	O2kLR-ArabianSea.Doose-Rolinski.2001	24.8	65.9	66	marine sediment	alkenone	PI/hist	loose
511	O2kLR-CapeChir.Kim.2007	30.9	-10.3	-10	marine sediment	alkenone	PI/hist	loose
512	O2kLR-CapeChir.McGregor.2007	30.8	-10.1	-10	marine sediment	alkenone	PI/hist	loose
513	O2kLR-CapeHatteras.Cloux.2012	35	-75.2	-75	marine sediment	foram Mg/Ca	PI/hist	strong/loose
514*	O2kLR-CariacoBasin.Black.2007	10.8	-64.8	-65	marine sediment	foram Mg/Ca	PI/hist	strong/loose
517	O2kLR-ChileanMargin.Lamy.2002	-41	-74.5	-74	marine sediment	alkenone	PI/hist	loose
518	O2kLR-DryTortugas.Lund.2006	24.6	-83.6	-84	marine sediment	foram Mg/Ca	PI/hist	loose

ID	Name	Lat	Lon	<i>Elev.masl</i>	Archive	Proxy	cutoff	selection
519	O2kLR-DryTortugasA.Lund.2006	24.3	-83.3	-83	marine sediment	foram Mg/Ca	PI/hist	loose
520	O2kLR-EasternTropicalNorthAtlantic.Kuhnert.2011	16.8	-16.7	-17	marine sediment	foram Mg/Ca	PI/hist	loose
521	O2kLR-EmeraldBasin.Keigwin.2003	45.9	-62.8	-63	marine sediment	alkenone	PI/hist	loose
523	O2kLR-FeniDriftRichter.2009	55.5	-13.9	-14	marine sediment	foram Mg/Ca	PI/hist	loose
524	O2kLR-FiskBasin.Richey.2009	27.6	-93.9	-94	marine sediment	foram Mg/Ca	PI/hist	strong/loose
525	O2kLR-GarrisonBasin.Richey.2009	26.7	-93.9	-94	marine sediment	foram Mg/Ca	hist	loose
526	O2kLR-GreatBahamaBank.Lund.2006	24.6	-79.3	-79	marine sediment	foram Mg/Ca	PI/hist	loose
527	O2kLR-GreatBahamaBankAtlantic0326aLund2006125MC	24.8	-79.3	-79	marine sediment	foram Mg/Ca	PI/hist	loose
528	O2kLR-GreatBarrier.Hendy.2002	-18.3	146.6	147	coral	Coral Sr/Ca	PI/hist	strong/loose
529	O2kLR-GulfofGuinea.Weldeab.2007	2.5	9.4	9	marine sediment	foram Mg/Ca	PI/hist	loose
530	O2kLR-JacatFjord.Sepulveda.2009	-44.3	-73	-73	marine sediment	alkenone	PI/hist	loose
532	O2kLR-KuroshioCurrent.Isono.2009	36	141.8	142	marine sediment	alkenone	PI/hist	loose
535	O2kLR-MakassarStrait-MD98-2177.Newton.2011	1.4	119.1	119	marine sediment	foram Mg/Ca	PI/hist	strong/loose
536	O2kLR-MakassarStrait.Linsley.2010	-7.4	115.2	115	marine sediment	foram Mg/Ca	PI/hist	loose
538	O2kLR-MakassarStrait.Oppo.2009	-3.5	119.2	119	marine sediment	foram Mg/Ca	PI/hist	loose
539	O2kLR-MD952011.Calvo.2002	67	7.6	8	marine sediment	alkenone	PI/hist	loose
540	O2kLR-Minorca.Moreno.2012	40.5	4	4	marine sediment	alkenone	PI/hist	loose
541*	O2kLR-NorthIceland.Sicre.2011	66.5	-17.4	-17	marine sediment	alkenone	PI/hist	strong/loose
542	O2kLR-NWPacific.Harada.2004	46.3	152.5	152	marine sediment	alkenone	PI/hist	loose
544	O2kLR-OkinawaTrough.Wu.2012	24.8	122.5	122	marine sediment	TEX86	PI/hist	loose
546	O2kLR-Philippines-MD98-2181.Stott.2007	6.3	125.8	126	marine sediment	foram Mg/Ca	PI/hist	loose
548	O2kLR-PigmyBasin.Richey.2009	27.2	-91.4	-91	marine sediment	foram Mg/Ca	PI/hist	strong/loose
550*	O2kLR-SantaBarbara.Zhao.2000	34.2	-120	-120	marine sediment	alkenone	PI/hist	strong/loose
551	O2kLR-SouthAtlantic.Leduc.2010	-29.1	16.7	17	marine sediment	alkenone	PI/hist	loose
552	O2kLR-SouthChinaSea.Zhao.2006	8.7	109.9	110	marine sediment	alkenone	PI/hist	loose
553	O2kLR-SouthernChile.Mohtadi.2007	-44.1	-75.2	-75	marine sediment	alkenone	PI/hist	loose
554*	O2kLR-SouthIceland.Sicre.2011	57.5	-27.9	-28	marine sediment	alkenone	PI/hist	strong/loose
555	O2kLR-SubTropicalEasternAtlantic.deMenocal.2000	20.8	-18.6	-19	marine sediment	planktonic foraminifera	PI/hist	loose
561	O2kLR-WesternSvalbard.Spielhagen.2011	78.9	6.8	7	marine sediment	planktonic foraminifera	PI/hist	loose
562	O2kLR-WestSpitzbergen.Bonnet.2010	79	5.9	6	marine sediment	dynocist MAT	PI/hist	loose
563	O2kLRMakassarStrait-MD98-2160.Newton.2011	-5.2	117.5	118	marine sediment	foram Mg/Ca	PI/hist	loose
654*	SAm-LagunaAculeo.vonGunten.2009	-33.9	-70.9	-71	lake sediment	reflectance	PI/hist	strong/loose
655*	SAm-LagunaChepical.deJong.2013	-32.3	-70.5	-70	lake sediment	reflectance	PI/hist	strong/loose
656*	SAm-LagunaEscondida.Elbert.2013	-45.5	-71.8	-72	lake sediment	BSi	PI/hist	strong/loose

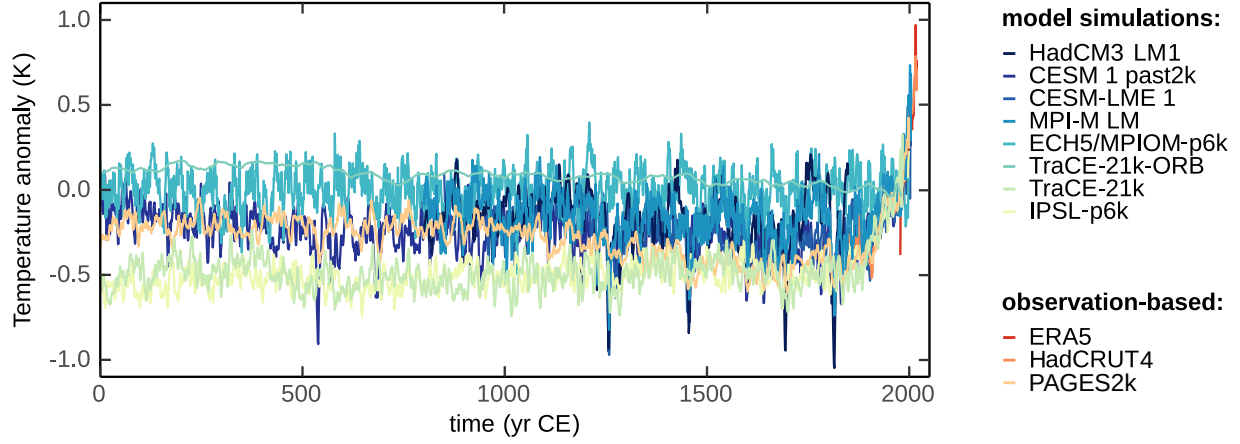


FIG. 1. Evolution of global mean temperature over the Common Era from model simulations and observation-based data as in Table I. Anomalies are given with respect to the reference period 1961-1990 (HadCM3 LM1:1800-1850) and as a running average of five years.

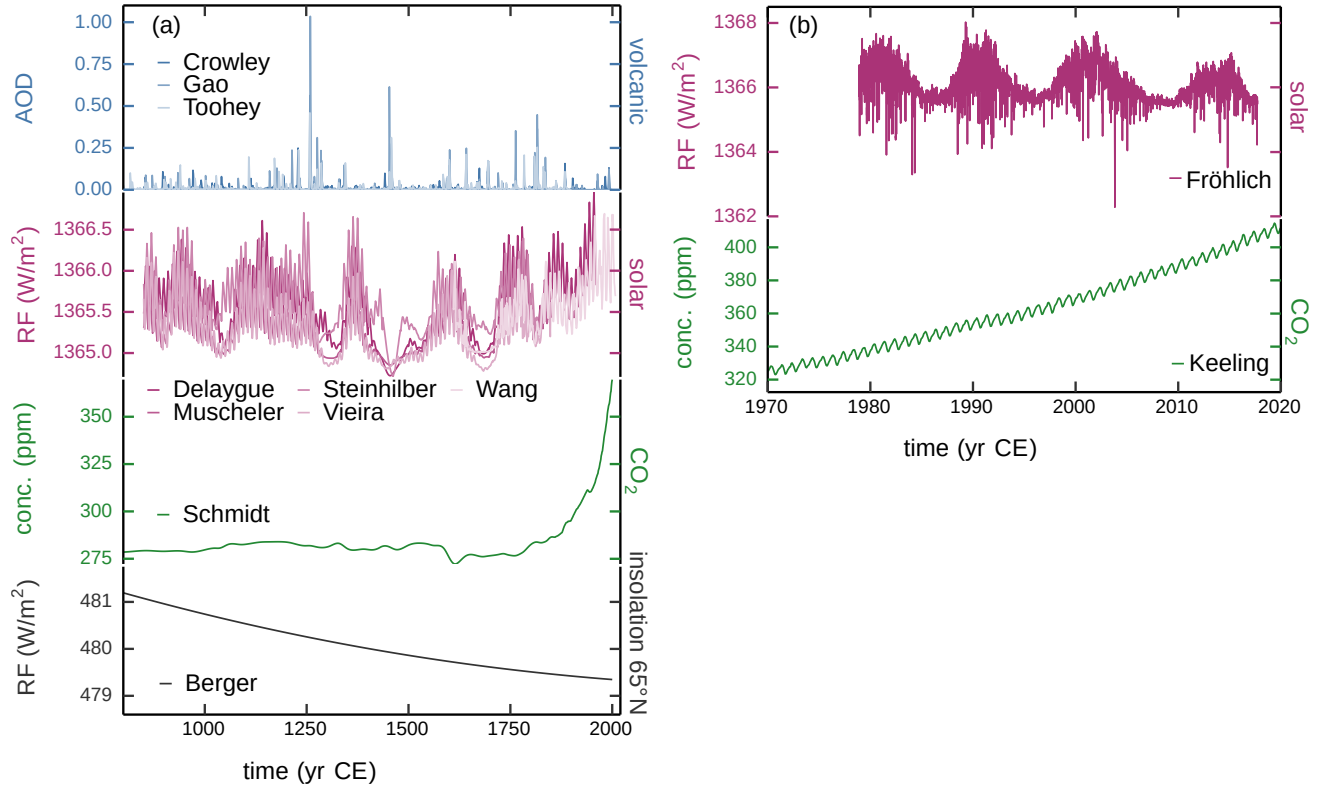


FIG. 2. (a) Reconstruction of climate drivers over the Common Era used to estimate the PSD of radiative forcing (RF). Labels indicate the data reference as given in Table II. (b) Additional observational data for solar and CO_2 forcing used to obtain high-frequency spectral estimates. Highly resolved insolation changes due to the diurnal and annual cycle are not shown here.

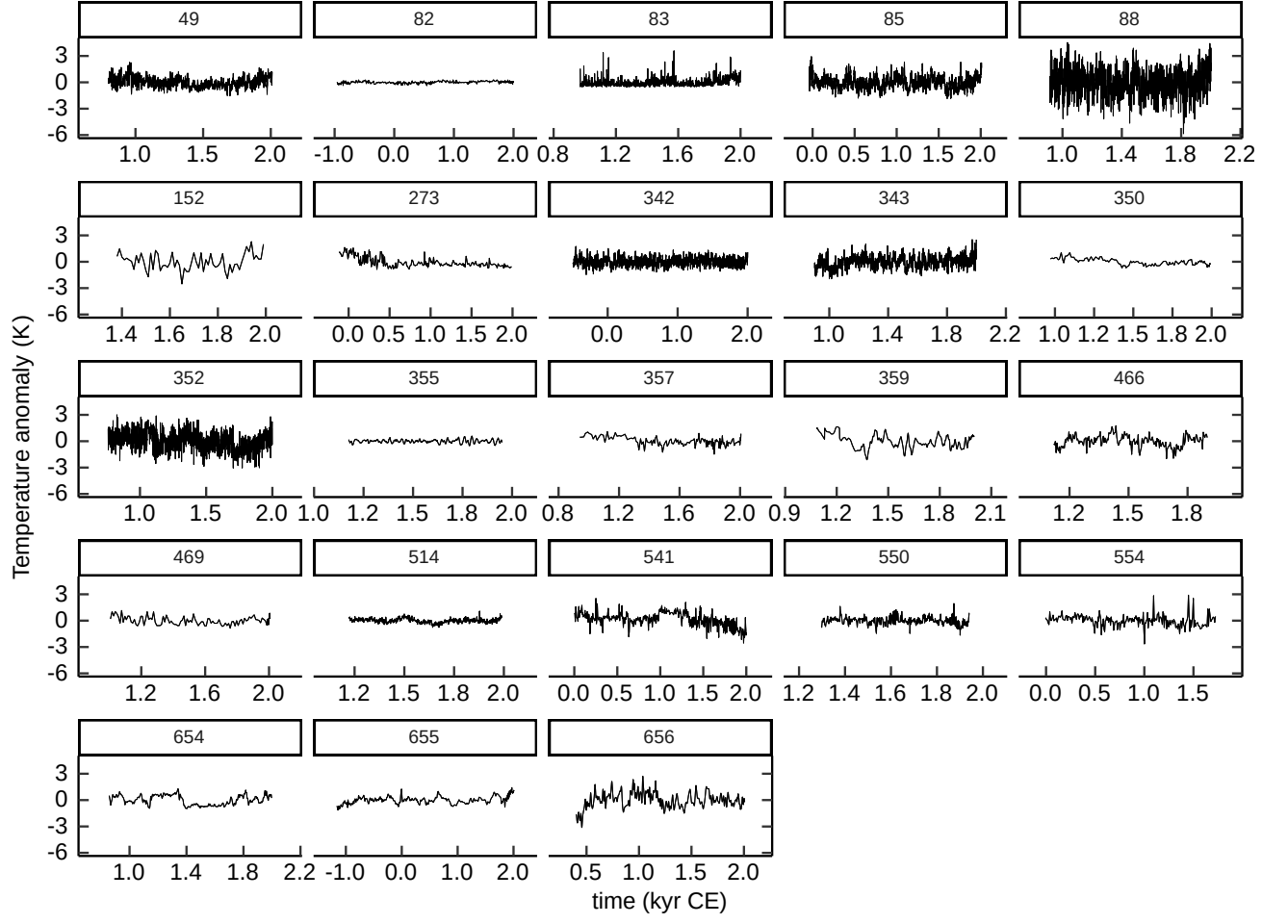


FIG. 3. Temperature anomalies from proxy records used to estimate local temperature variability. The labels give the ID from the PAGES2k database as indicated by a star (\star) in Table III.

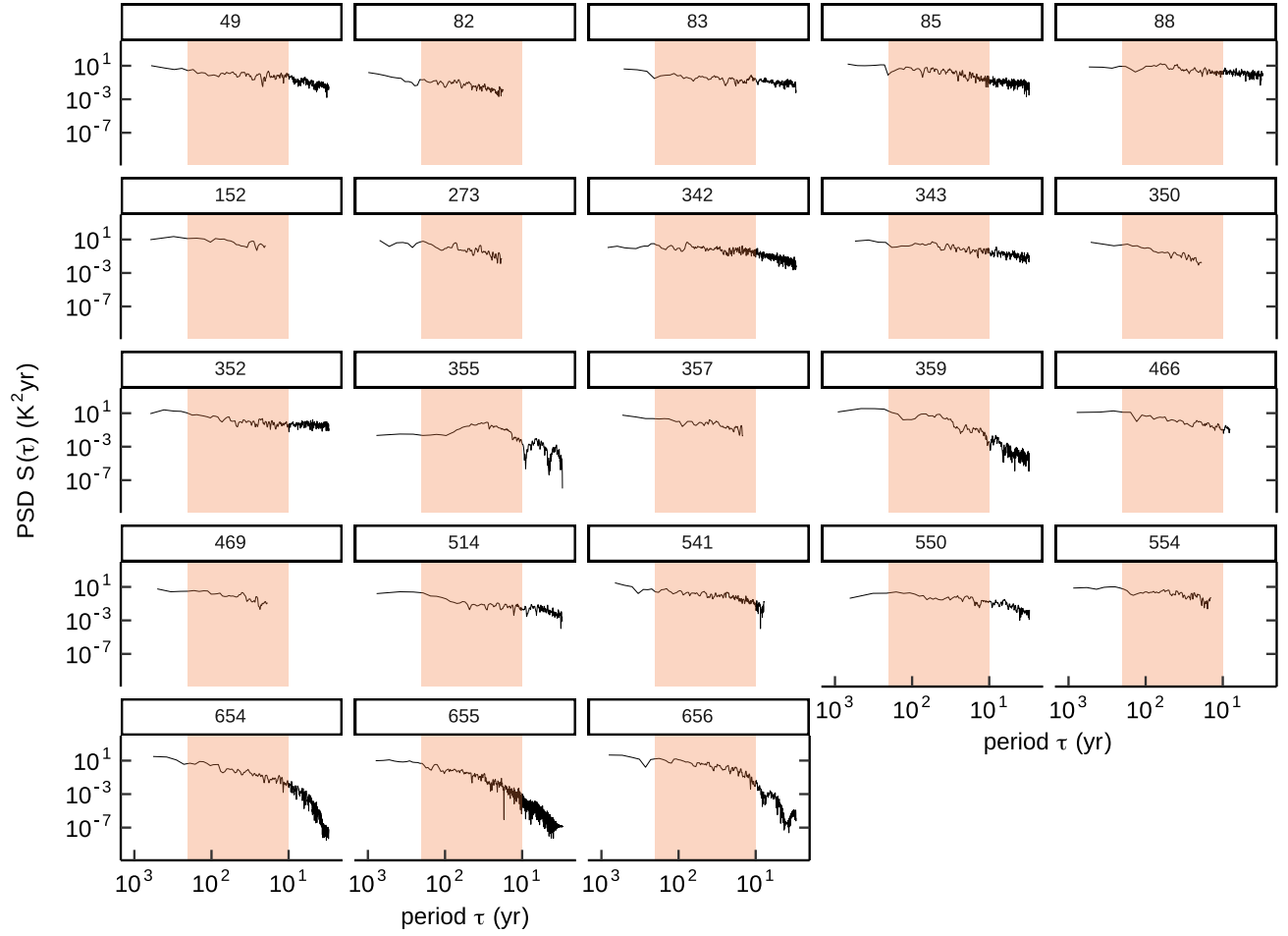


FIG. 4. As Figure 3, but showing the PSD of the proxy records. The shaded area indicates the periods between 10 and 200 years, used to estimate the scaling relationship. Scaling exponents for spectra that do not cover the full period were estimated on their corresponding timescales, but at least between 20 and 200 years.

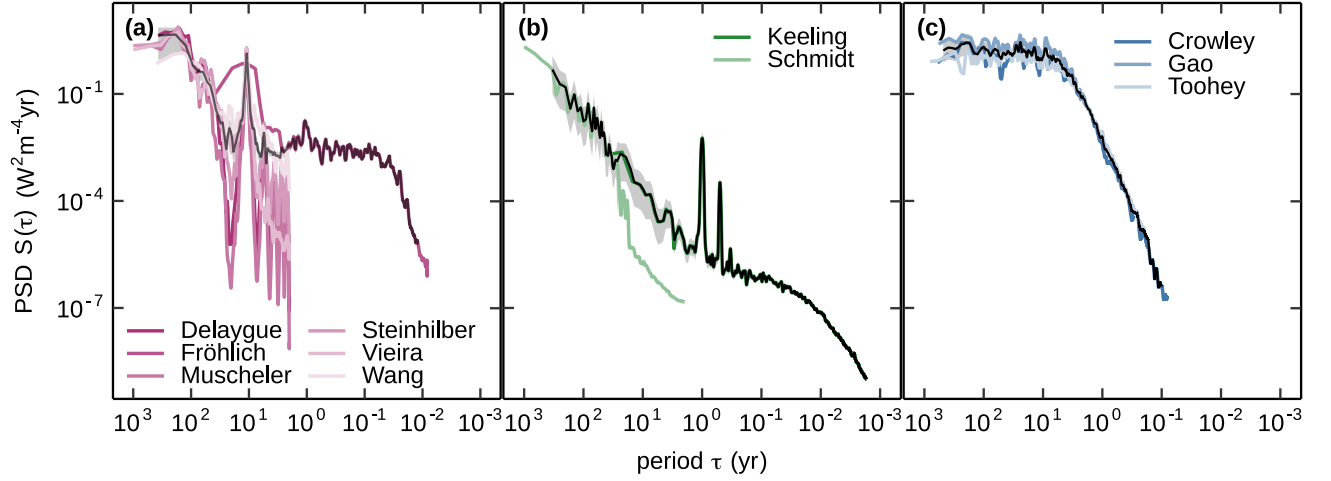


FIG. 5. Power spectral densities of solar (a), CO₂ (b), and volcanic (c) from multiple data sets and their mean spectra (black). Low- and high-frequency tails, likely prone to spectral biases, were omitted in the average.

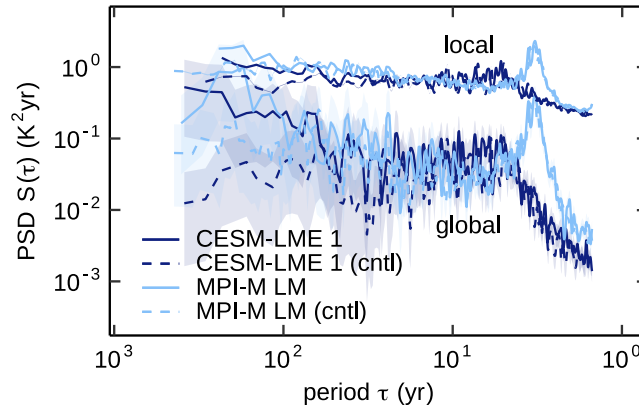


FIG. 6. PSD for global mean and mean of local spectra of surface air temperature from last millennium runs and their PI control (cntl).

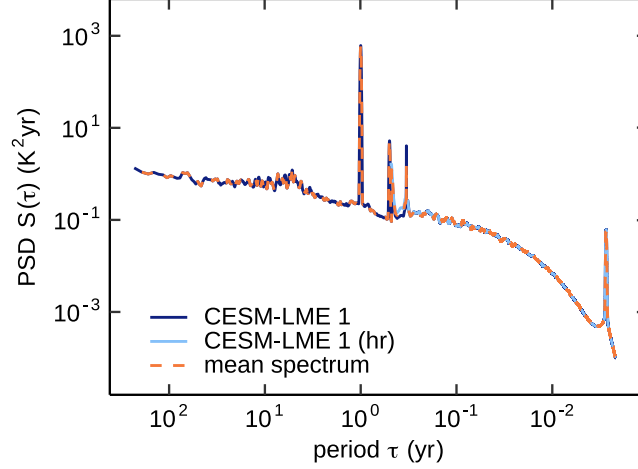


FIG. 7. Joint PSD (dashed orange line) from the mean spectrum of a highly (hr) and lower resolved time series on the example of surface air temperature from the CESM-LME 1 run. To improve computational efficiency, we formed this joint PSD for ERA5, MPI-M LM, and CESM-LME 1. The high-frequency component was estimated from data at hourly resolved temperature series from 1981 to 1990 CE since this is a part of the climatic period that is shared among the three data sets.

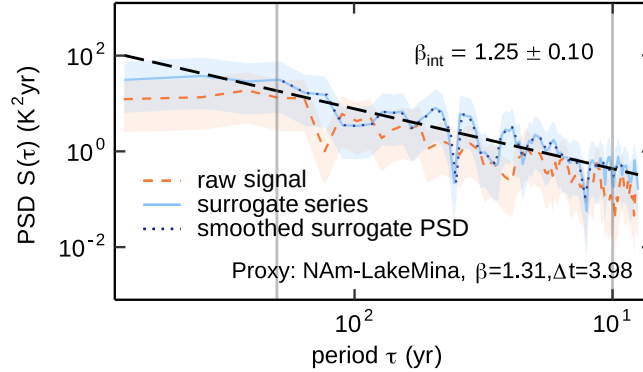


FIG. 8. Step-wise estimation of uncertainty on β -scaling relation for irregularly sampled proxy records on the example of the PSD from the “NAM-LakeMina”-record. When interpolated to its mean temporal resolution Δt , the raw signal has a scaling relation $\beta = 1.31$ (orange dashed line). The uncertainties were calculated from 100 surrogates that are random time series with approximately the same power-law scaling β (black dotted line). The PSD is altered after forming the block-average of the surrogate time series and interpolation to Δt (blue solid line). Linear regression on this spectrum (black dashed line) gives the scaling coefficient β_{int} of the surrogate series.

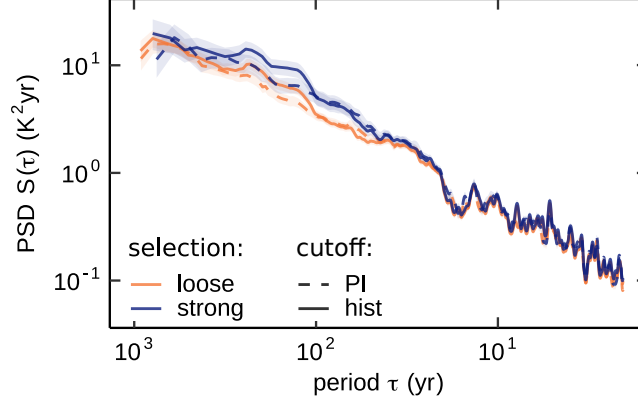


FIG. 9. Global mean of local PSD from proxy records subject to sampling from the PAGES2k data base and global warming. Dashed and solid lines refer to the mean spectra of local proxy records cut at 1850 CE (PI) and 2000 CE (hist) respectively. The plot compares strong (blue) and loose (orange) criteria. Loose criteria are described in the data section of the main manuscript and were used to calculate the mean of local spectra from reconstructions. For the stronger criteria we require the mean temporal resolution ($\langle t_{i+1} - t_i \rangle \leq 20$ years), a coverage $(t_N - t_1) \geq 30$ years and the number of data points $N \geq 30$. Hiatus are tolerated up to $\max(t_{i+1} - t_i) \geq 40$ years.

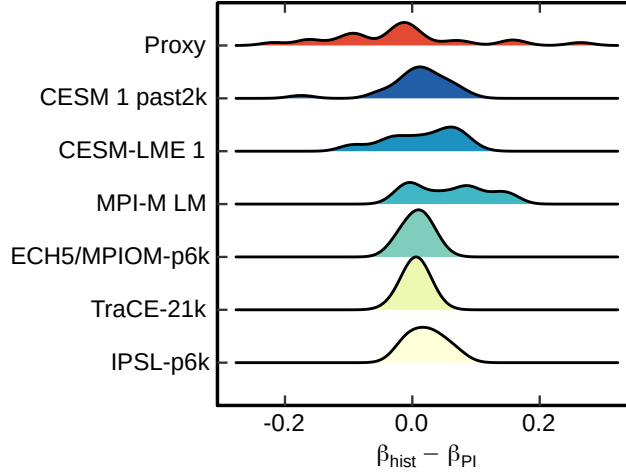


FIG. 10. Normalized density plots of the deviations of the spectral exponent β extracted from time series up to 2020 CE (β_{hist}) and time series up to 1850 CE (β_{PI}). The densities were computed from the local power-law scaling used to estimate the statistical agreement between models and data (Table III).

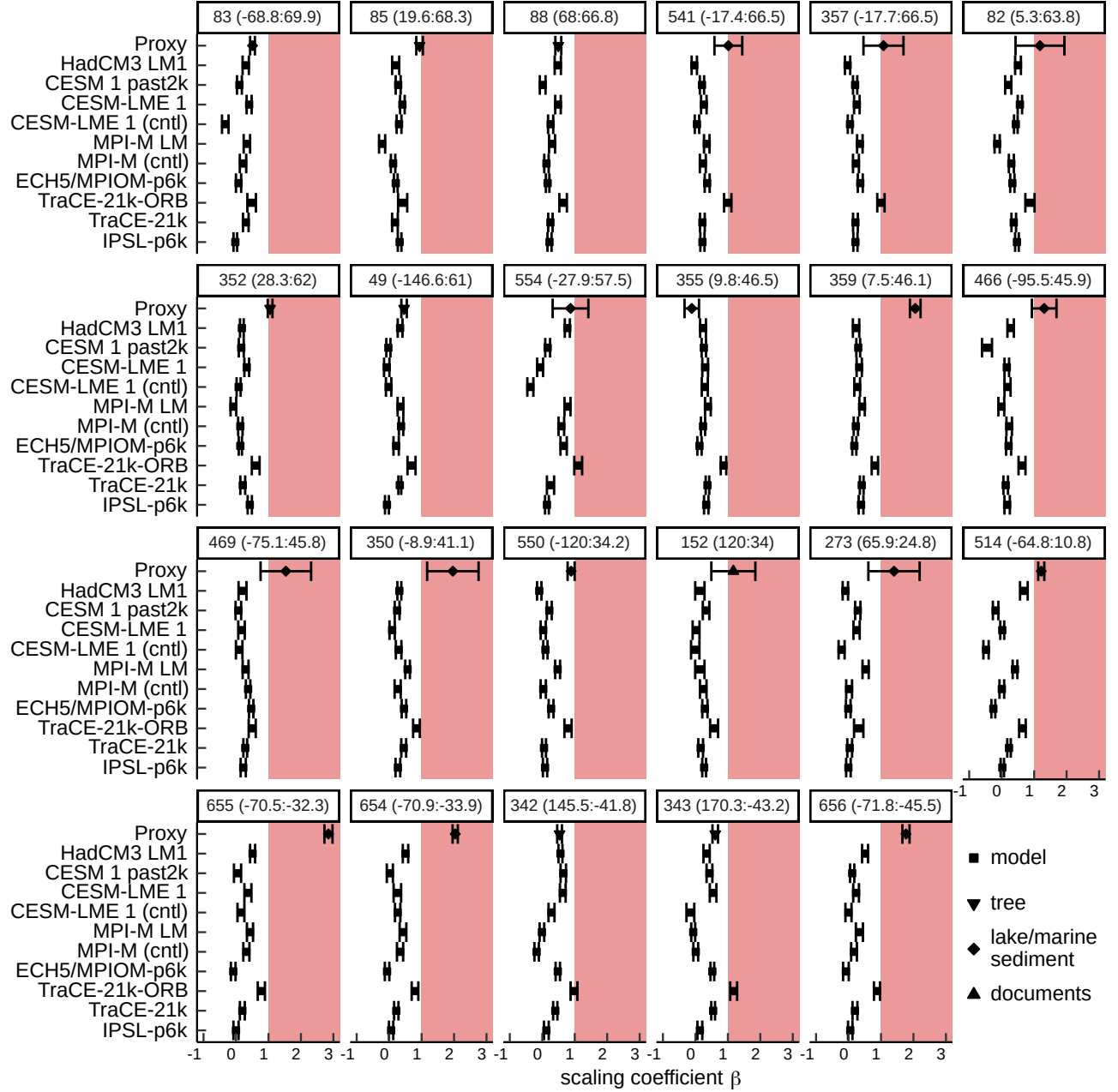


FIG. 11. Local scaling coefficients and its confidence intervals from simulations and paleoclimate data. Each panel denotes the ID within the PAGES2k database and its coordinates (longitude °E, latitude °N). Symbols indicate the archive of the proxy record or whether the scaling exponent belongs to a model simulation or not. Red shading refers to scaling exponents $\beta > 1$, whereas the white background indicates $\beta < 1$.

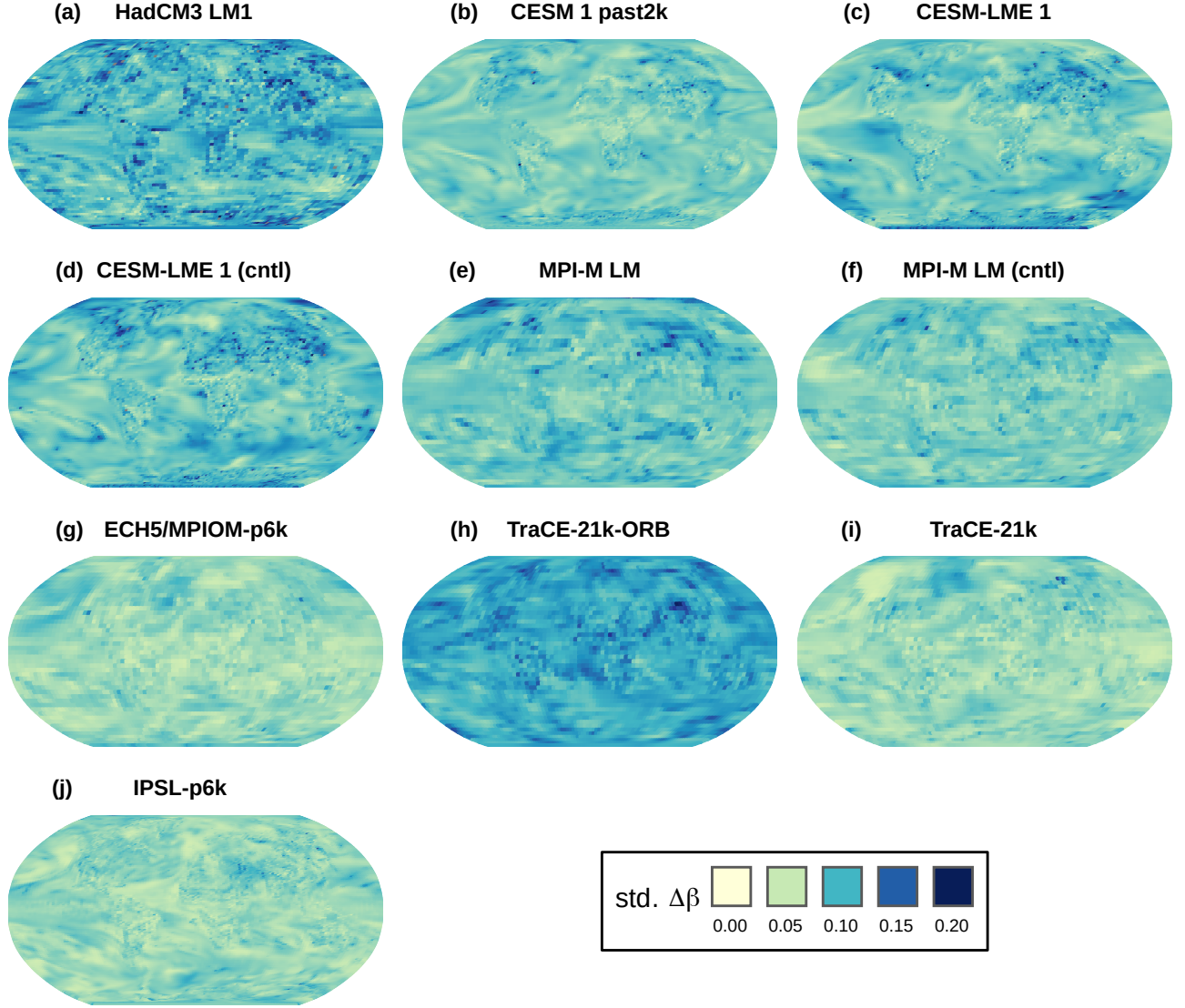


FIG. 12. Standard deviation of the least-square regression of local scaling coefficient β for all model simulations. The goodness of fit is generally lower for models with a comparatively low temporal resolution (Trace21k-ORB) or coverage (HadCM3 LM1). Furthermore, there is a slightly increased deviation in areas of active modes of variability, such as the ENSO region ((b), (c), (e), (j)). This could be due to the fact, that spectral peaks describe these (quasi-)periodic signals better than power-law scaling.

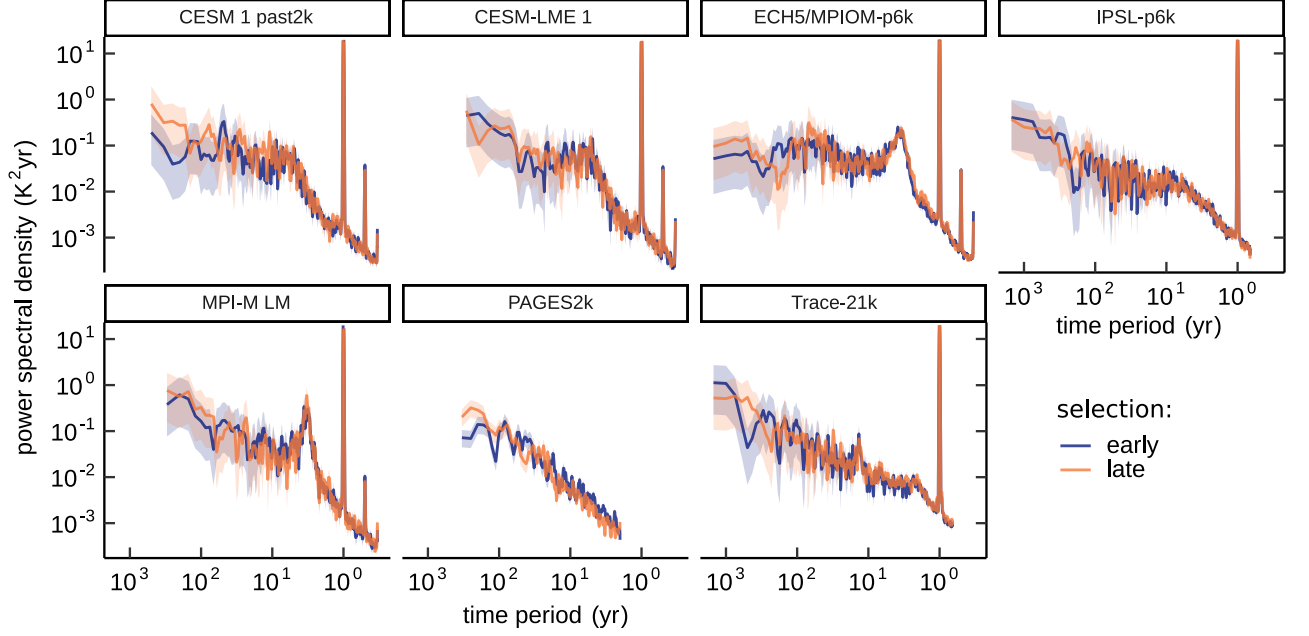


FIG. 13. PSD of global mean surface temperature from model simulations and PAGES2k reconstruction. To test the robustness of our spectral analysis against potentially non-trending, non-stationary signals in the data sets, each temperature signal was split into two disjoint time intervals of equal length, representing the “early” and the “late” part of the signal. The latter contains the anthropogenic global warming period, starting approximately 1850 CE. Trace-21k-ORB (orbitally forced only) as well as HadCM3 LM1 (800-1850 CE) were excluded from the discussion since they do not represent the recent global warming.

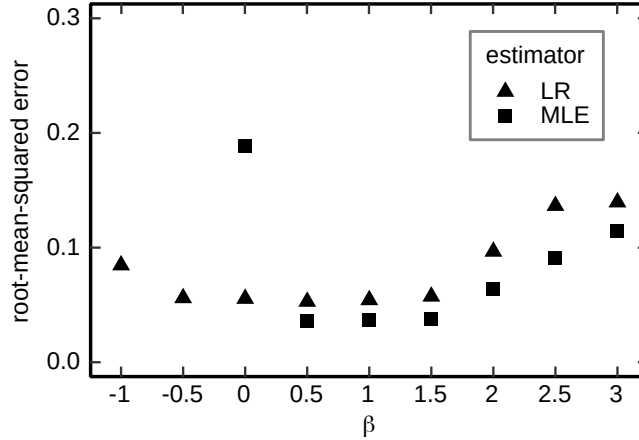


FIG. 14. Root-mean-squared error of linear regression (LR) and maximum likelihood estimation (MLE) [1, 2] computed from 200 surrogate time series with 6000 data points and power-law scaling β . The grey dashed line marks the mean confidence $\Delta\beta_{\text{LR}}$ of the linear regression. Outliers (> 0.3) of the MLE for negative scaling exponents are not shown here. The implemented (standard) MLE is generally not appropriate to estimate $\beta \leq 0$, which explains deviations in this range [2].

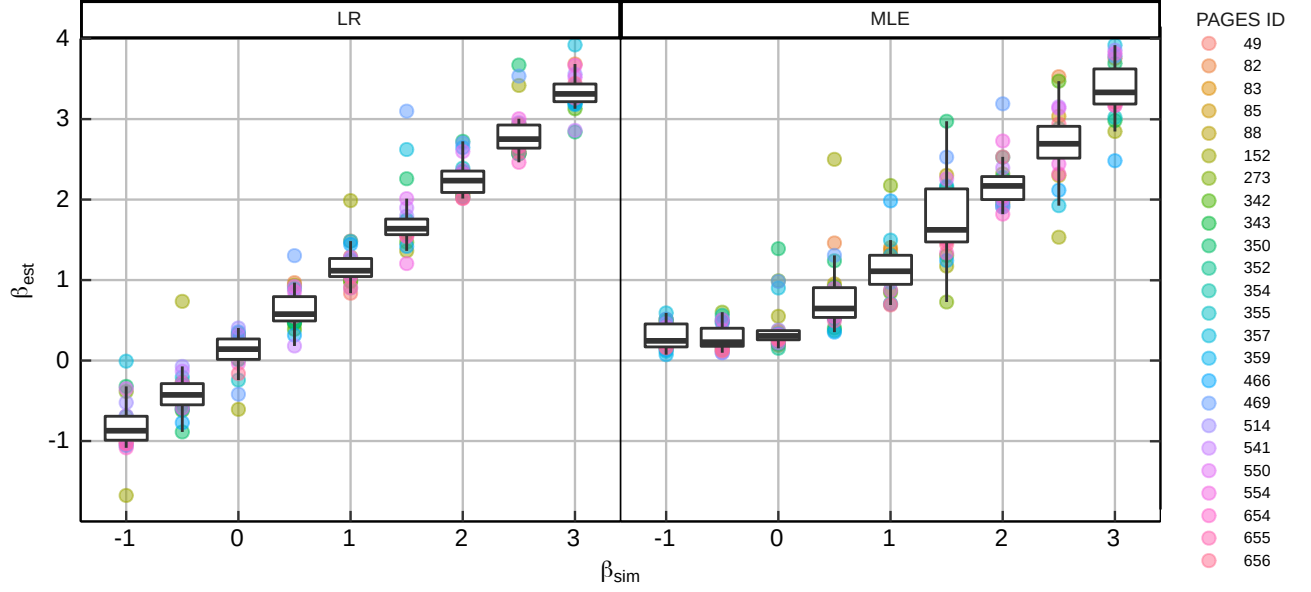


FIG. 15. Distribution of estimated beta (β_{est}) from irregularly sampled pseudo proxy records using LR and MLE. For each possible β_{sim} , a set of 200 surrogate time series was block-averaged to the resolution of each proxy record before computing its power spectral density. The horizontal thick lines within the boxes correspond to the median. The ends of the box denote the upper (75%) and lower (25%) quartiles. The vertical line extends from the upper ending of the box to the largest value no further than 1.5 times the interquartile range, and vice versa for the lower bound. Points further outside are potential outliers, of which the IDs 152, 273, 350, and 469 can be explained by their comparatively low mean resolution of 9-10 years.

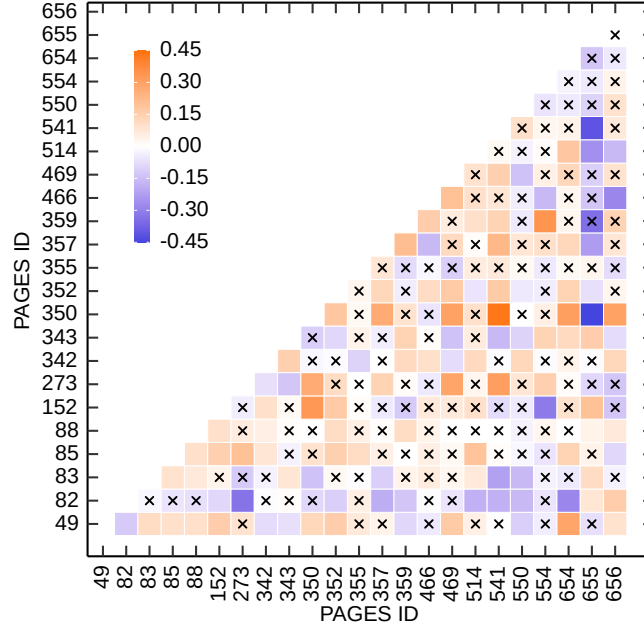


FIG. 16. Cross-correlations among the 23 proxy records, denoted by the ID of the PAGES2k database [3]. Insignificant correlations are marked by a cross. The cross-correlations for the irregularly sampled data were computed using the *nest*-package [4, 5] in R.

-
- [1] C. Gillespie, powerLaw - Package (R) (2020).
 - [2] A. Clauset, C. R. Shalizi, and M. E. J. Newman, Power-law distributions in empirical data, *SIAM Review* **51**, 661–703 (2009).
 - [3] PAGES 2k Consortium., Consistent multidecadal variability in global temperature reconstructions and simulations over the Common Era, *Nature Geoscience* **12**, 643 (2019).
 - [4] K. Rehfeld, N. Marwan, J. Heitzig, and J. Kurths, Comparison of correlation analysis techniques for irregularly sampled time series, *Nonlinear Processes in Geophysics* 10.5194/npg-18-389-2011 (2011).
 - [5] K. Rehfeld and J. Kurths, Similarity estimators for irregular and age-uncertain time series, *Climate of the Past* , 107 (2014).
 - [6] Y. Zhong, A. Jahn, G. H. Miller, and A. Geirsdottir, Asymmetric Cooling of the Atlantic and Pacific Arctic During the Past Two Millennia: A Dual Observation-Modeling Study, *Geophysical Research Letters* **45**, 12,412 (2018).
 - [7] J. H. Jungclauss et al., The PMIP4 contribution to CMIP6 – Part 3: The last millennium, scientific objective, and experimental design for the PMIP4 simulations, *Geoscientific Model Development* **10**, 4005 (2017).
 - [8] B. L. Otto-Bliesner, E. C. Brady, J. Fasullo, A. Jahn, L. Landrum, S. Stevenson, N. Rosenbloom, A. Mai, and G. Strand, Climate variability and change since 850 ce an ensemble approach with the community earth system model, *Bulletin of the American Meteorological Society* 10.1175/BAMS-D-14-00233.1 (2016).
 - [9] G. A. Schmidt et al., Climate forcing reconstructions for use in PMIP simulations of the last millennium (v1.0), *Geoscientific Model Development* **4**, 33 (2011).
 - [10] J. H. Jungclauss et al., Climate and carbon-cycle variability over the last millennium, *Climate of the Past* 10.5194/cp-6-723-2010 (2010).
 - [11] J. C. Böhler, C. Roesch, M. Kirschner, L. Sime, M. D. Holloway, and K. Rehfeld, Comparison of the oxygen isotope signatures in speleothem records and iHadCM3 model simulations for the last millennium, *Climate of the Past Discussions* **2020**, 1 (2020).
 - [12] A. P. Schurer, S. F. B. Tett, and G. C. Hegerl, Small influence of solar variability on climate over the past millennium, *Nature Geoscience* **7**, 104 (2014).
 - [13] P. Braconnot, D. Zhu, O. Marti, and J. Servonnat, Strengths and challenges for transient Mid-to Late Holocene simulations with dynamical vegetation, *Climate of the Past* **15**, 997 (2019).
 - [14] Z. Liu, Transient simulation of last deglaciation with a new mechanism for Bølling–Allerød warming, *Science* **325**, 10.1126/science.1171041 (2009).
 - [15] A. L. Berger, Long-term variations of daily insolation and Quaternary climatic changes., *Journal of Atmospheric Sciences* 10.1175/1520-0469(1978)035<2362:ltvodi>2.0.co;2 (1978).
 - [16] F. Joos and R. Spahni, Rates of change in natural and anthropogenic radiative forcing over the past 20,000 years, *Proceedings of the National Academy of Sciences* **105**, 1425 LP (2008).
 - [17] N. Fischer and J. H. Jungclauss, Evolution of the seasonal temperature cycle in a transient Holocene simulation: Orbital forcing and sea-ice, *Climate of the Past* 10.5194/cp-7-1139-2011 (2011).
 - [18] H. Hersbach, B. Bell, P. Berrisford, and S. Hirahara, The ERA5 global reanalysis, *Quarterly*

- Journal of the Royal Meteorological Society , 1999 (2020).
- [19] C. P. Morice, J. J. Kennedy, N. A. Rayner, and P. D. Jones, Quantifying uncertainties in global and regional temperature change using an ensemble of observational estimates: The Had-CRUT4 data set, *Journal of Geophysical Research Atmospheres* **117**, 10.1029/2011JD017187 (2012).
 - [20] G. A. Schmidt et al., Climate forcing reconstructions for use in PMIP simulations of the Last Millennium (v1.1), *Geoscientific Model Development* **5**, 185 (2012).
 - [21] T. J. Crowley and M. B. Unterman, Technical details concerning development of a 1200 yr proxy index for global volcanism, *Earth System Science Data* **5**, 187 (2013).
 - [22] C. Gao, A. Robock, and C. Ammann, Volcanic forcing of climate over the past 1500 years: An improved ice core-based index for climate models, *Journal of Geophysical Research: Atmospheres* **113**, 10.1029/2008JD010239 (2008).
 - [23] M. Toohey and M. Sigl, Reconstructed volcanic stratospheric sulfur injections and aerosol optical depth, 500 BCE to 1900 CE, version 2, World Data Center for Climate (WDCC) at DKRZ 10.1594/WDCC/eVol2k_v2 (2017).
 - [24] G. Delaygue and E. Bard, An Antarctic view of Beryllium-10 and solar activity for the past millennium, *Climate Dynamics* **36**, 2201 (2011).
 - [25] R. Muscheler, F. Joos, J. Beer, S. A. Müller, M. Vonmoos, and I. Snowball, Solar activity during the last 1000yr inferred from radionuclide records, *Quaternary Science Reviews* **26**, 82 (2007).
 - [26] F. Steinhilber, J. Beer, and C. Fröhlich, Total solar irradiance during the Holocene, *Geophysical Research Letters* **36**, 10.1029/2009GL040142 (2009).
 - [27] L. E. Vieira and S. K. Solanki, Evolution of the solar magnetic flux on time scales of years to millenia, *Astronomy and Astrophysics* 10.1051/0004-6361/200913276 (2010).
 - [28] N. A. Krivova, L. Balmaceda, and S. K. Solanki, Reconstruction of solar total irradiance since 1700 from the surface magnetic flux, *Astronomy and Astrophysics* 10.1051/0004-6361:20066725 (2007).
 - [29] Y. Wang, J. L. Lean, and N. R. Sheeley, Jr., Modeling the Sun’s Magnetic Field and Irradiance since 1713, *The Astrophysical Journal* 10.1086/429689 (2005).
 - [30] C. Fröhlich, Solar irradiance variability since 1978: Revision of the PMOD composite during solar cycle 21, *Space Science Reviews* **125**, 53 (2006).
 - [31] C. D. Keeling, R. B. Bacastow, and A. E. Bainbridge, Atmospheric carbon dioxide variations at Mauna Loa Observatory, Hawaii, *TELLUS* 10.3402/tellusa.v28i6.11322 (1976).
 - [32] M. Crucifix, Palinsol - Package (R) (2016).